




Reciprocal priming between receptor tyrosine kinases at recycling endosomes orchestrates cellular signalling outputs

Michael P Smith^{1,†}, Harriet R Ferguson^{1,†} , Jennifer Ferguson¹, Egor Zindy^{2,‡}, Katarzyna M Kowalczyk^{1,§}, Thomas Kedward³, Christian Bates¹, Joseph Parsons³, Joanne Watson⁴, Sarah Chandler¹ , Paul Fullwood¹, Stacey Warwood⁵, David Knight⁵, Robert B Clarke^{3,6} & Chiara Francavilla^{1,6,*} 

Abstract

Integration of signalling downstream of individual receptor tyrosine kinases (RTKs) is crucial to fine-tune cellular homeostasis during development and in pathological conditions, including breast cancer. However, how signalling integration is regulated and whether the endocytic fate of single receptors controls such signalling integration remains poorly elucidated. Combining quantitative phosphoproteomics and targeted assays, we generated a detailed picture of recycling-dependent fibroblast growth factor (FGF) signalling in breast cancer cells, with a focus on distinct FGF receptors (FGFRs). We discovered reciprocal priming between FGFRs and epidermal growth factor (EGF) receptor (EGFR) that is coordinated at recycling endosomes. FGFR recycling ligands induce EGFR phosphorylation on threonine 693. This phosphorylation event alters both FGFR and EGFR trafficking and primes FGFR-mediated proliferation but not cell invasion. In turn, FGFR signalling primes EGF-mediated outputs via EGFR threonine 693 phosphorylation. This reciprocal priming between distinct families of RTKs from recycling endosomes exemplifies a novel signalling integration hub where recycling endosomes orchestrate cellular behaviour. Therefore, targeting reciprocal priming over individual receptors may improve personalized therapies in breast and other cancers.

Keywords fibroblast growth factor receptor; quantitative phosphoproteomics; receptor tyrosine kinases; signalling; trafficking

Subject Categories Membranes & Trafficking; Proteomics; Signal Transduction

DOI 10.15252/emboj.2020107182 | Received 29 October 2020 | Revised 27 April 2021 | Accepted 28 April 2021

The EMBO Journal (2021) e107182

Introduction

Receptor tyrosine kinases (RTKs), such as fibroblast growth factor (FGF) and epidermal growth factor (EGF) receptors, respond to perturbations in the environment by initiating signalling cascades in proximity to the plasma membrane upon binding of their growth factors (Wintheiser & Silberstein, 2020). Ligand-induced proximal or early signalling is then amplified through cascades—such as the mitogen-activated protein kinase (ERK, p38), phosphoinositide 3-kinase (PI3K) and phospholipase C γ (PLC γ) pathways—specifies cell fate and controls cellular homeostasis during development and in pathological conditions (Lemmon & Schlessinger, 2010). Indeed, deregulated early signalling and signalling rewiring are responsible for unwanted long-term outputs, such as increased proliferation and motility, in human diseases, including cancer (Du & Lovly, 2018). This is the main reason why signalling molecules are the target of most of the known cancer therapies (Yaffe, 2019). However, each RTK is not an isolated entity on the plasma membrane, but functions within complex networks with other RTKs to fine-tune cancer cell intracellular signalling and long-term fate decisions. Indeed, targeting single molecules is often not enough to switch off unwanted cancer cell responses, as highlighted for instance in breast cancer (Harbeck *et al*, 2019). Recent advances in mass spectrometry (MS)-based phosphoproteomics allows us to simultaneously analyse thousands of signalling molecules and their post-translational modifications (PTMs) (Huang, 2012; Doll *et al*, 2019; Lundby *et al*, 2019; Bludau & Aebersold, 2020). However, how different RTK families integrate their downstream signalling has not been comprehensively analysed yet. A better understanding of the molecular mechanisms used by RTKs to coordinate each other's signalling architecture will help to identify how to interfere with the right target at the right

1 Division of Molecular and Cellular Function, School of Biological Science, Faculty of Biology Medicine and Health (FBMH), The University of Manchester, Manchester, UK

2 Division of Cell Matrix and Regenerative Medicine, School of Biological Science, FBMH, The University of Manchester, Manchester, UK

3 Division of Cancer Sciences, School of Medical Science, FBMH, The University of Manchester, Manchester, UK

4 Division of Evolution and Genomic Sciences, School of Biological Science, FBMH, The University of Manchester, Manchester, UK

5 Bio-MS Core Research Facility, FBMH, The University of Manchester, Manchester, UK

6 Manchester Breast Centre, Manchester Cancer Research Centre, Manchester, UK

*Corresponding author. Tel: +44 161 275 5208; E-mail: chiara.francavilla@manchester.ac.uk

[†]These authors contributed equally to this work

[‡]Present address: Center for Microscopy and Molecular Imaging, Université Libre de Bruxelles (ULB), Gosselies, Belgium

[§]Present address: Department of Biochemistry, University of Oxford, Oxford, UK

time to re-direct deregulated cancer cell behaviours. This idea would also support the current therapeutic concept in breast cancer aiming at personalized combination of therapies at early stage of treatment prior to the acquisition of resistance or to delay it (Harbeck *et al*, 2019).

Multiple mechanisms contribute to shape signalling architecture, including the nature and affinity of the receptor ligand (Zinkle & Mohammadi, 2019), receptor co-activation (Tan *et al*, 2017), feedback mechanisms (Nguyen & Kholodenko, 2016) and the spatio-temporal distribution of signalling transducers (Bergeron *et al*, 2016). Ligand-dependent endocytic trafficking (hereafter trafficking) of RTKs from and to the plasma membrane regulates early signalling and downstream responses (Goh & Sorkin, 2013; Schmid, 2017; Budick-Harmelin & Miaczynska, 2018). For instance, we have shown that fibroblast growth factor 10 (FGF10) and transforming growth factor α (TGF α) initiate specific early signalling events that regulate FGFR2b and EGFR recycling to the plasma membrane, respectively, resulting in enhanced cell motility (Francavilla *et al*, 2013; Francavilla *et al*, 2016). It is, however, unknown whether ligand-induced recycling plays a role in the signalling interplay between RTKs to coordinate long-term responses. This concept is supported by alterations in the ability of cancer cells to migrate and proliferate due to derailed RTK trafficking (Mellman & Yarden, 2013; Lanzetti & Di Fiore, 2017) and by EGFR/integrin recycling-dependent regulation of cancer cell migration (Caswell & Norman, 2008).

Here, to study how ligand-induced trafficking—and more specifically recycling to the plasma membrane—affected signalling coordination downstream from FGFRs in breast cancer cells we combined quantitative phosphoproteomics and targeted assays. FGFRs are a large family of RTKs composed of alternatively spliced isoforms of four genes (*Fgfr1b-c*, *Fgfr2b-c*, *Fgfr3b-c*, *Fgfr4*), where the “b” and “c” isoforms are expressed mainly on epithelial and mesenchymal cells, respectively (Ornitz & Itoh, 2015). More than 22 FGF ligands exist (Ornitz & Itoh, 2015), making FGF/FGFR an ideal system to study trafficking-dependent signalling integration. FGFRs play an important yet understudied role in breast cancer and are deregulated in a significant percentage of the oestrogen/progesterone receptor (ER/PR) and triple-negative breast cancer (TNBC) subtypes of breast cancer (Babina & Turner, 2017; Navid *et al*, 2020). Furthermore, FGFs are essential for proficient breast cancer organoid growth (Sachs *et al*, 2018), but their role *in vivo* is less clear (Clayton & Grose, 2018; Watson & Francavilla, 2018; Navid *et al*, 2020). Although breast cancer is known to have deregulated RTK signalling and trafficking (Butti *et al*, 2018), the functional consequences of recycling in breast cancer cells are yet to be determined. It is also unclear how ligand, receptor, and protein adaptors integrate trafficking and signalling to fine-tune breast cancer cellular responses. Therefore, to dissect recycling-dependent integration of signalling outputs from multiple angles, we developed three quantitative trafficking phosphoproteomics approaches (TPAs), which focused on recycling FGFs-, recycling FGFRs- and recycling adaptor-dependent signalling (Fig 1A). To our knowledge, previous global studies of the trafficking-signalling enigma focused on a single question, either uncovering general trafficking regulators by genetic screening or multiparametric imaging analysis (Collinet *et al*, 2010; Liberali *et al*, 2014; Gut *et al*, 2018) or revealing the partners of

trafficking effectors by proximity labelling methods (Gillingham *et al*, 2019). Here, we constructed for the first time a snapshot of FGFR recycling-dependent signalling in breast cancer cells and provided a comprehensive resource for the trafficking, signalling and cancer communities. We unexpectedly identified a novel signalling interplay between FGFR and EGFR from the recycling endosomes. Specifically, FGFR recycling ligands induce phosphorylation on EGFR at the non-catalytic threonine T693 (T669 in the UniProt sequence P00533) that reciprocally affects both FGFR and EGFR signalling outputs in breast cancer cells. We have therefore elucidated reciprocal priming between FGFR and EGFR which is based on an early phosphorylation-dependent signal and which coordinates trafficking-dependent signalling outputs.

Results

TPAs unmask FGFR-dependent EGFR_T693 phosphorylation

To investigate recycling-dependent signalling in breast cancer cells, we compared the FGFR2b recycling stimulus FGF10 to FGF7, which induces FGFR2b degradation (Francavilla *et al*, 2013) (Fig 1B and C, Appendix Fig S1A and B), and analysed changes in the global signalling of a panel of five FGFR2b-expressing breast cancer cell lines (Francavilla *et al*, 2013) (Appendix Fig S1C). The breast cancer cell lines were treated with FGF7 or FGF10 for 1 or 8 min., and such early signalling was analysed using phosphoproteomics, hereafter referred to as trafficking phosphoproteomics approach 1 (TPA1) (Fig 1A). TPA1 showed a high degree of reproducibility in four independent experiments with the identification of phosphorylated peptides in the high intensity range and the quantification of 4559 proteins and 9494 phosphorylated sites in total, consistent with previous publications (Lundby *et al*, 2019) (Appendix Fig S1C–I, Datasets EV1 and EV2). Hierarchical clustering of the differentially regulated phosphorylated sites showed clustering of breast cancer cell lines based on their known molecular subtypes (Neve *et al*, 2006), within which we identified clusters based on FGFR2b-specific early signalling (Appendix Fig S2A). We focused on the 5 cell line-specific FGFR2b signalling clusters identified across the breast cancer cell lines (32.5% of the phosphoproteome) and found an enrichment for proteins involved in signalling pathways, adhesion and establishment of localization (endocytosis and transport) common to all cell lines (Appendix Fig S2B). Within these 5 clusters, 78 kinases were identified as being phosphorylated (Appendix Fig S2C) and 12 of them were associated with the Gene Ontology (GO) terms establishment of localization and/or adhesion—including EGFR—consistent with enrichment of all proteins (Appendix Fig S2B and C). To study the differential phosphoproteomes downstream from FGF7 and FGF10, we focused on T47D and BT20. Each cell line represents a distinct breast cancer molecular subtype (Neve *et al*, 2006), mirrored in FGFR2b-specific clusters (Appendix Fig S2A). Furthermore, these cell lines express different levels of *Fgfr2b* (Appendix Fig S2D) and respond to FGF7/10 stimulation, as shown by increasing phosphorylation of ERK and cell proliferation (Watson & Francavilla, 2018) (Fig 1D, Appendix Fig S2E–G). Interestingly, hierarchical clustering showed that each FGF separated the phosphoproteome to a greater extent than the duration of stimulation (Fig 1E and F, Appendix Fig S2H and I),

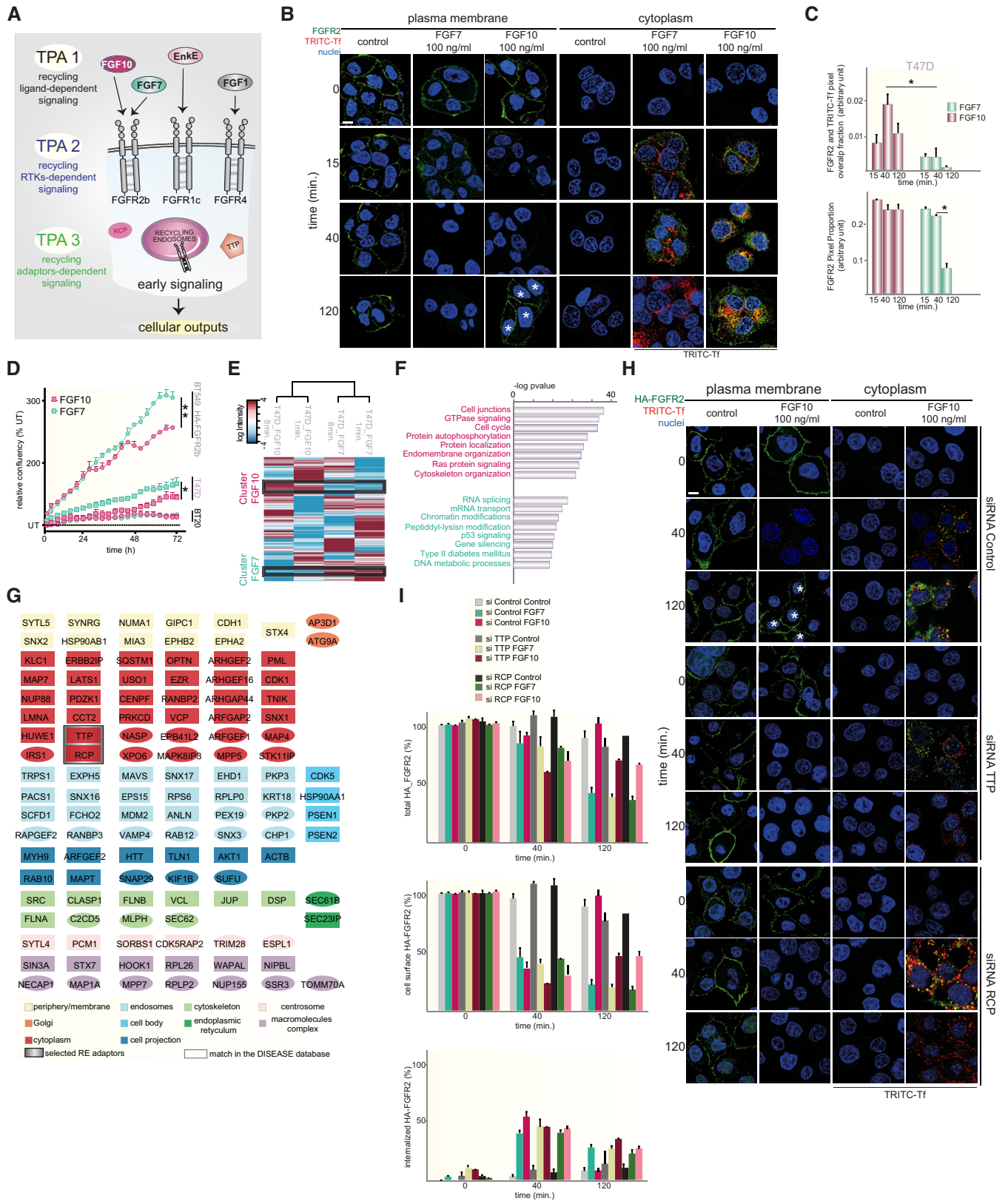


Figure 1.

Figure 1. Trafficking phosphoproteomics reveals FGFR2b recycling-dependent outputs.

- A Overview of the trafficking phosphoproteomic approaches (TPAs).
- B Internalization (cytoplasm) and recycling (plasma membrane) of FGF7- and FGF10-stimulated endogenous FGFR2 (green) for 0, 15, 40, and 120 min. in T47D. TRITC-Tf is a marker of recycling (red). Nuclei are stained in blue. *, cells with receptor recycled to the plasma membrane. Scale bar, 5 μ m.
- C Red and green pixels overlap fraction representing the co-localization of FGFR2b with the recycling endosomes marker Tf (above) and the proportion of green over total pixels representing FGFR2b in the cytoplasm (below) upon stimulation with FGF7 (dark green) or FGF10 (burgundy) for 15, 40, or 120 min. Values represent the median \pm SD of at least 3 independent experiments. Representative pictures are shown in B (cytoplasm). * $P < 0.005$ (Student's *t*-test).
- D Confluence over time of BT20, T47D, and BT549 transfected with HA-FGFR2b stimulated with FGF7 (dark green) or FGF10 (burgundy). Data represent the mean \pm SD of $N = 3$ compared with FGF10. $P = < 0.05^*$, $< 0.01^{**}$, $< 0.001^{***}$ (Student's *t*-test).
- E Hierarchical clustering of the phosphorylated sites differentially quantified T47D stimulated with FGF7 (green) or FGF10 (burgundy). Specific clusters are highlighted with black lines. The intensity of phosphorylated sites is presented on the logarithmic scale with intensity below and above the mean colour-coded in blue and red, respectively.
- F Enriched terms in the selected clusters of E, cluster FGF10 (burgundy, top), cluster FGF7 (green, bottom).
- G Network of phosphorylated proteins belonging to "protein localization" in FGF10 clusters, based on STRING, visualized in Cytoscape, and colour-coded based on cell components. The squared shape represents phosphorylated proteins found in the database DISEASES. The recycling adaptors TTP and RCP are highlighted in grey.
- H Internalization (cytoplasm) and recycling (plasma membrane) of FGF10-stimulated HA-FGFR2b (green) transfected in BT549 stimulated for 0, 40 and 120 min. Cells were depleted or not of TTP or RCP by a pool of siRNAs. TRITC-Tf is a marker of recycling (red). Nuclei are stained in blue. *, cells with receptor recycled to the plasma membrane. Scale bar, 5 μ m.
- I The presence (total), internalization (internalized) and recycling (cell surface) of transfected HA-FGFR2b in BT549 upon stimulation were quantified as in (Francavilla *et al*, 2016) and in the section "Quantification of the Recycling assay". Values represent the median \pm SD of $N = 3$. Representative pictures upon FGF10 stimulation are shown in H.

confirming the uniqueness of ligand responses (Francavilla *et al*, 2013). Analysis of the FGF7- and FGF10-specific clusters showed enrichment of the GO term protein localization unique to FGF10 stimulation in both T47D and BT20 (Fig 1E and F, Appendix Fig S2H and I). In support of the idea that the FGF10 phosphoproteome regulates protein localization in breast cancer cells, we found that the FGF10 phosphorylated proteins were enriched in all cellular compartments including endosomes and that 63% of them were ascribed to human diseases, including breast cancer (Pletscher-Frankild *et al*, 2015; Fig 1G). Furthermore, the FGF10-regulated phosphoproteome in T47D and BT20 contained TTP and RCP (Fig 1G), known to regulate FGFR2b and EGFR recycling, respectively (Francavilla *et al*, 2013; Francavilla *et al*, 2016). Confocal microscopy confirmed that FGF10-induced FGFR2b recycling required TTP (Francavilla *et al*, 2013), but also RCP (Fig 1H and I, Appendix Fig S2J). Altogether, these data highlight a role for TTP and RCP in FGFR2b trafficking and early signalling specifically induced by the recycling ligand FGF10 in breast cancer cells.

Next, we studied how widely recycling affects signalling in breast cancer cells by assessing the contribution of three recycling FGFRs and of the recycling adaptors TTP and RCP to changes in the phosphoproteome, hereafter referred to as TPA2 and TPA3, respectively (Fig 1A, Datasets EV3–EV5). TPA2 compares the signalling downstream of recycling FGFRs in a defined genetic background. We overexpressed FGFR1c, 2b, or 4 in BT549 cells, which lack these FGFRs, and stimulated cells with Enkamin-E, FGF10, or FGF1 for 8 and 40 min., respectively (Fig 2A). It is known that each of these ligands induced recycling of the paired receptor (Haugsten *et al*, 2005; Francavilla *et al*, 2013; Francavilla *et al*, 2016) and we showed also ligand-dependent sustained signalling activation (Appendix Fig S3A and B). Hierarchical clustering of the 6402 phosphorylated sites from this high-quality dataset (Appendix Fig S3C–H) identified a cluster related to early signalling (8 min) and one associated with late endosomal signalling (40 min.) common to all the considered FGFR-ligand pairs (Fig 2B). Refined analysis of this recycling receptor cluster revealed

a signalling network of 866 proteins of which 38 were known trafficking proteins and 24, among which EGFR, TTP and RCP, were also identified by TPA1 (Figs 1 and 2C, and Appendix Figs S1–S3I). TPA3 analysed the FGF10-dependent phosphoproteome of T47D in the presence or absence of the recycling adaptors TTP or RCP (Fig 2D, Appendix Fig S3J). We identified 9569 phosphorylated sites and verified the high level of correlation between replicates of TPA3 (Appendix Fig S1–O). Hierarchical clustering identified TTP- and RCP-specific clusters and a common recycling adaptor cluster (Fig 2E). The analysis of 113 proteins associated with the GO term establishment of localization in the latter cluster revealed 22 proteins already identified by TPA1, of which 6 were kinases, including EGFR (Figs 1 and 2F, and Appendix Figs S1, S2 and S3P). To identify key regulators of signalling downstream from FGFR recycling in breast cancer cells based on the multi-angle TPAs, we focused on phosphorylated proteins belonging to the GO term establishment of localization and prioritized the 22 phosphorylated proteins in common to the three TPAs (Fig 2G). This group of proteins included scaffolding proteins and the three protein kinases AKT, PAK1 and, strikingly, EGFR (Fig 2G). Assessment of EGFR-phosphorylated sites that were differentially regulated within each TPA highlighted that the phosphorylation of the non-catalytic threonine 693 (EGFR_T693) was uniquely associated with a recycling signature (40 min. upon stimulation) (Fig 2G). Therefore, the three quantitative TPAs developed to study FGFR recycling-dependent signalling integration in breast cancer cells (Fig 1A) unveiled a FGFR recycling-associated EGFR_T693 phosphorylation (Figs 1G, 2C, F, G and Datasets EV1–EV5). This finding suggests a hitherto unknown signalling interplay between FGFRs and EGFR in breast cancer cells. As EGFR_T693 phosphorylation is critical for EGF-induced EGFR internalization (Heisermann *et al*, 1990) and is induced by the EGFR recycling stimulus TGF α in a sustained manner (Francavilla *et al*, 2016), we hypothesized that EGFR_T693 phosphorylation may contribute towards FGFR outputs that depend on FGFR recycling.

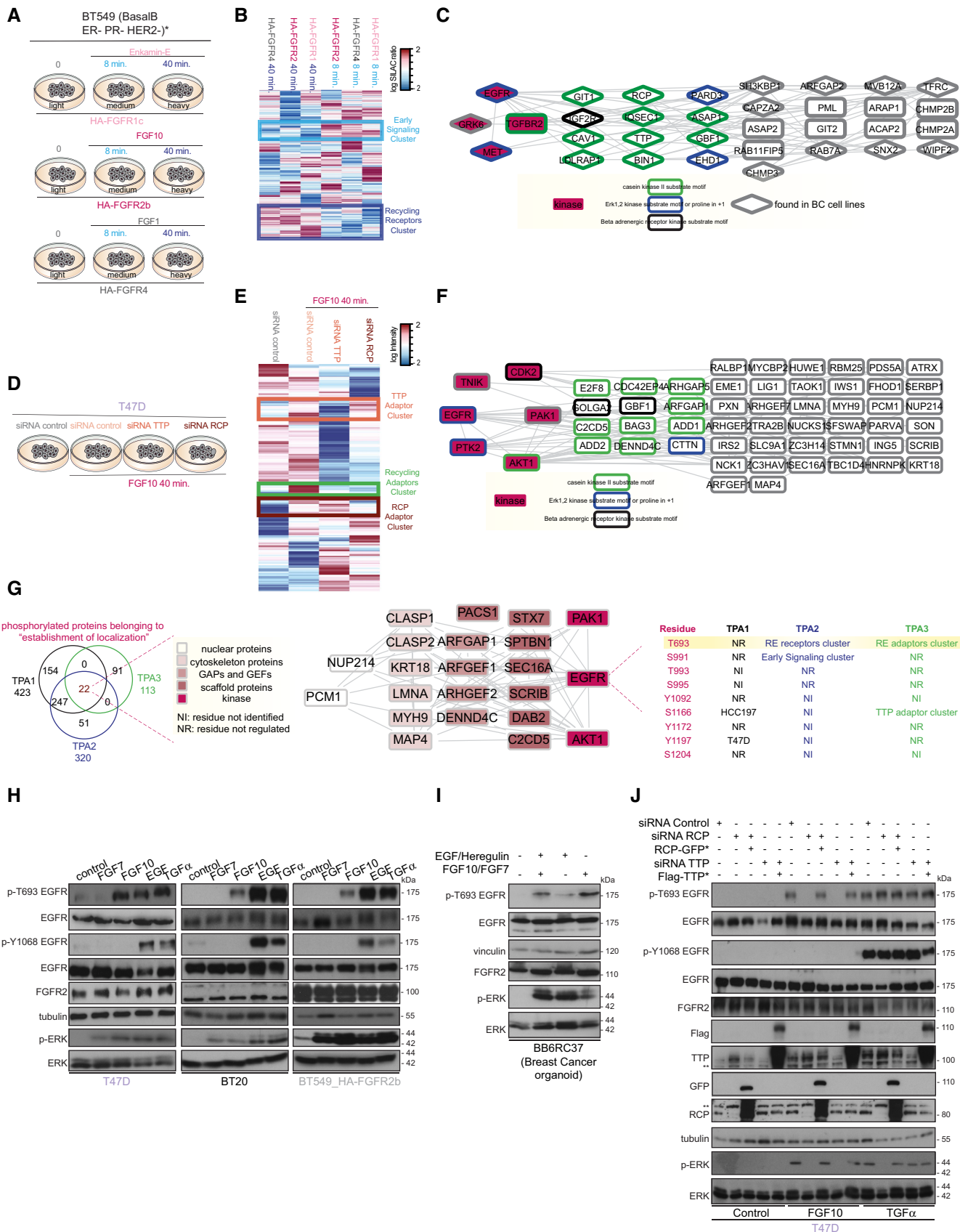


Figure 2.

Figure 2. TPA2-3 unveil FGF10-dependent EGFR_T693 phosphorylation.

- A Experimental design of TPA2.
- B Hierarchical clustering of the phosphorylated sites differentially quantified in BT549 transfected with HA-FGFR1c, 2b or 4 and stimulated for 8 or 40 min. with Enkamin-E, FGF10 or FGF1, respectively. Early signalling and recycling receptor clusters are highlighted in light and medium blue, respectively. The intensity of phosphorylated sites is presented on the logarithmic scale with intensity below and above the mean colour-coded in blue and red, respectively.
- C STRING-based and Cytoscape-visualized network of the phosphorylated proteins belonging to “endocytosis” (clusters medium blue in b). The diamond shape represents phosphorylated proteins found in TPA1. Kinases are highlighted in burgundy. The border is colour-coded based on the substrate motifs.
- D Experimental design of TPA3.
- E Hierarchical clustering of the phosphorylated sites differentially quantified in T47D stimulated with FGF10 and depleted or not of TTP or RCP. The clusters for TTP adaptors, RCP adaptors or recycling adaptors are highlighted in orange, brown and light green, respectively. The intensity of phosphorylated sites is presented on the logarithmic scale with intensity below and above the mean colour-coded in blue and red, respectively.
- F STRING-based and Cytoscape-visualized network of phosphorylated proteins belonging to the recycling adaptor cluster (light green in E) and found in TPA1. Kinases are highlighted in burgundy. The border is colour-coded based on the substrate motifs.
- G Venn diagram showing the phosphorylated proteins belonging to “establishment of localization” identified in TPA1-3 (left). STRING-based and Cytoscape-visualized network of the 22 proteins identified by the 3 TPAs (centre). Phosphorylated sites quantified on EGFR (right). T693 is highlighted in yellow.
- H–J Lysates from (H) T47D, BT20 and HA-FGFR2b-transfected BT549 stimulated or not with FGF7, FGF10, EGF and TGF α for 40 min; (I) breast cancer organoid cultured from the PDX tumour BB6RC37 and grown for the last 24 h as indicated; (J) control or 40 min. FGF10- or TGF α -stimulated T47D left untreated or depleted of TTP, followed or not by transfection with siRNA-resistant Flag-TTP (Flag-TTP*) or depleted of RCP followed or not by transfection with siRNA-resistant RCP-GFP (RCP-GFP*) were immunoblotted with the indicated antibodies. **, non-specific band (J).

EGFR_T693 phosphorylation is FGFR2b ligand-, recycling- and activation-dependent

To verify the potential interplay between FGFR and EGFR, we first validated EGFR_T693 phosphorylation in T47D, BT20, HA-FGFR2b-BT549 and a breast cancer organoid grown from a TNBC patient-derived xenograft (PDX) tumour (Eyre *et al*, 2016). FGF10, but not FGF7, induced EGFR phosphorylation on T693, whilst leaving the catalytic residue tyrosine 1068 (Y1068) unaltered at 40-min. stimulation (Maennling *et al*, 2019). By contrast, the EGFR ligands EGF and TGF α induced the phosphorylation of both T693 and Y1068, as shown previously (Ceresa & Peterson, 2014) (Fig 2H and I). Therefore, sole phosphorylation of EGFR at T693 is FGF10/FGFR2b-specific.

To confirm that FGF10-induced FGFR2b recycling was involved in EGFR_T693 phosphorylation, we depleted TTP or RCP and stimulated T47D and BT20 with FGF10 for 40 min. This resulted in decreased EGFR_T693 phosphorylation and ERK activation upon depletion of either recycling adaptor (Appendix Fig S4A and B). Overexpressing siRNA-resistant TTP or RCP restored both EGFR_T693 phosphorylation and ERK phosphorylation following FGF10 stimulation (Fig 2J). Furthermore, we observed a peak in EGFR_T693 phosphorylation at 40 min. post-stimulation with FGF10 when FGFR2b was present in recycling endosomes (Fig 1B–I, Appendix Fig S4C). Finally, FGF10-mediated phosphorylation of EGFR_T693 decreased when FGFR2b trafficking was inhibited by dominant-negative Rab11 (preventing recycling) or dominant-negative dynamin (preventing internalization) with no discernible alterations in ERK activation (Appendix Fig S4D–G). As TGF α or EGF-induced EGFR_T693 phosphorylation occurs regardless of length of stimulation, or trafficking inhibition (Fig 2J, Appendix Fig S4), we concluded that EGFR_T693 phosphorylation is independent of EGFR recycling, but FGFR2b-induced phosphorylation of EGFR on T693 requires recycling upon FGF10 stimulation.

We next verified whether the kinase activity of FGFR was required for EGFR_T693 phosphorylation. Enkamin-E, FGF10 and FGF1 induced EGFR_T693 phosphorylation in cells expressing their cognate receptors, but this was suppressed by the FGFR inhibitor PD173074 (Pardo *et al*, 2009) (Fig 3A and B). Similarly,

FGF10-dependent EGFR_T693 phosphorylation decreased in cells transfected with the catalytically inactive HA-FGFR2b_Y656F/Y657F (Francavilla *et al*, 2013) (Fig 3C). Furthermore, FGF10, but not TGF α , required FGFR activation to induce EGFR_T693 phosphorylation and ERK activation in breast cancer cells expressing endogenous FGFR2b (Fig 3D). Conversely, TGF α -, but not FGF10-induced EGFR_T693 phosphorylation was blocked by the EGFR inhibitor AG1478 (Han *et al*, 1996) (Fig 3D). These data suggest that EGFR_T693 phosphorylation downstream from FGFR ligands depends on FGFR but not EGFR activation. As a conserved proline follows T693 on EGFR and TPA2-3 uncovered an ERK-kinase-substrate (or proline in +1) motif encompassing the phosphorylated EGFR (Figs 2 C–F and 3E), we treated T47D and BT20 with MEK inhibitors, U0126 and MEK162 (Cheng & Tian, 2017), or the p38 kinase inhibitor BMS582949 (Emami *et al*, 2015) (Fig 3A). Both MEK inhibitors blocked ERK phosphorylation in cells stimulated with FGF10 and TGF α , and EGFR_T693 phosphorylation was simultaneously decreased upon FGF10 treatment, and to lesser extent upon TGF α , whereas p38 inhibition had no effect (Fig 3F–G). Therefore, EGFR_T693 phosphorylation depended on MEK-ERK, but not p38, signalling upon FGF10 stimulation.

In conclusion, FGF ligands which induce the recycling of their paired FGFR receptor increase EGFR_T693 phosphorylation via FGFR and ERK signalling, independent of EGFR or p38 activity.

FGF10 primes EGFR responses

To explore the consequences of the FGFR and EGFR interplay, we first tested the effect of FGF10 on EGFR functions. FGF10 stimulation did not alter the levels of EGFR, which decrease over time upon EGF—and to a lesser extent TGF α —stimulation (Francavilla *et al*, 2016) (Fig 4A). However, if T47D cells were pre-treated for 40 min with FGF10, followed by stimulation with EGF for different time points, we observed an increase in EGFR abundance and ERK activation relative to cells not pre-treated with FGF10 for 120 min (Fig 4 B). FGF10 pre-treatment did not have the same effect on EGFR stabilization from the recycling stimulus TGF α at 120 min and a less pronounced effect on ERK phosphorylation at any time point. These data suggest that FGF10 pre-treatment alters EGF signalling to increase stability of EGFR at 120 min resulting in higher levels of

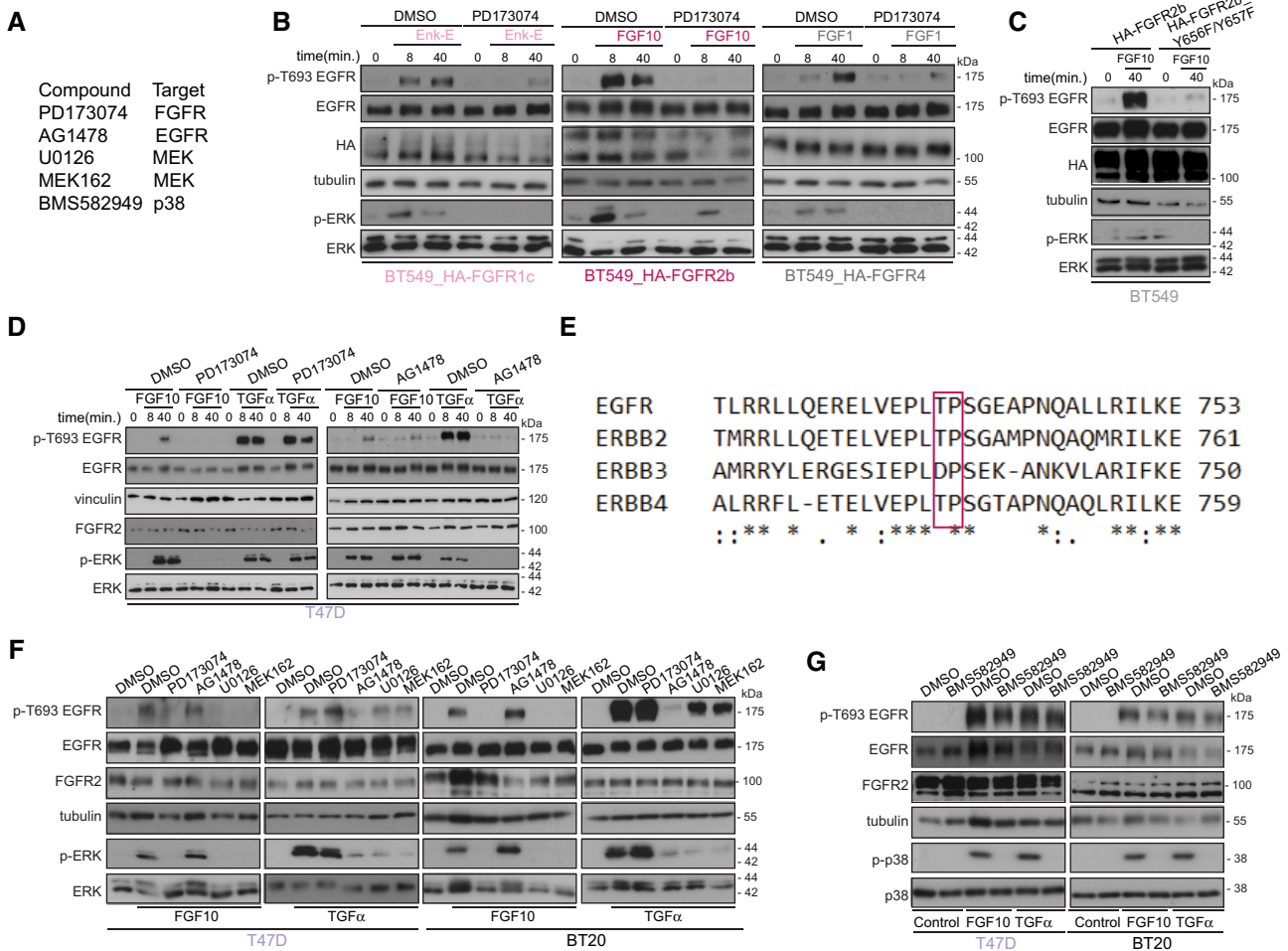


Figure 3. FGF10-dependent EGFR_T693 phosphorylation requires FGFR and ERK.

A List of compounds and their targets.
B–D Lysates from BT549 transfected with HA-FGFR1c, 2b, or 4 and stimulated for 8 or 40 min with Enkamin-E, FGF10 or FGF1, respectively, followed by treatment with either DMSO or the FGFR inhibitor PD173074 (**B**); BT549 transfected with HA-FGFR2b or HA-FGFR2b_Y656F/Y657F and stimulated with FGF10 for 40 min. (**C**); T47D treated with DMSO, PD173074 or the EGFR inhibitor AG1478 and stimulated or not with either FGF10 or TGFα for 0, 8 and 40 min. (**D**) were immunoblotted with the indicated antibodies.
E Protein sequences surrounding T693 (based on UniProt P00533) of members of the ErbB family were aligned using CLUSTAL O (version 1.2.4). The red box indicates that the amino acid T is followed by a conserved proline. Asterisks below the sequences indicate identical amino acid residues; double dots indicate conserved amino acid residues; single dots indicate semi-conserved substitutions.
F, G Lysates from T47D or BT20 treated with DMSO, PD173074, AG1478 or the MEK inhibitors U0126 and MEK162 and stimulated or not with either FGF10 or TGFα (**F**); T47D or BT20 treated with DMSO, or the p38 inhibitor BMS582949 and stimulated or not with either FGF10 or TGFα (**G**) were immunoblotted with the indicated antibodies.

ERK activation. FGFR2 levels remained high with all treatment conditions; however 40 min., FGF10 pre-treatment did alter the dynamics of FGFR2b downstream of both EGF and TGFα stimulation. The effect of FGF10 pre-treatment on EGFR dynamics in EGF-stimulated cells depended on both FGFR and ERK activities (Fig 4C and D). When EGFR was stabilized with AG1468 (Gan *et al*, 2007), the stability of the EGFR following pre-treatment was in line with FGF10 40-min stimulation, whereas ERK activation decreased (Fig 4E). Therefore, FGF10 pre-treatment increases the total levels of EGFR after EGF stimulation, and this resulted in sustained ERK phosphorylation, an effect dependent on the activation of the FGFR-ERK signalling axis. Correspondingly, FGF10 pre-treatment followed

by EGF stimulation for 4h induced the highest expression of ERK late target genes (Uhlitz *et al*, 2017) (Fig 4F), which may suggest enhanced cell cycle progression (Sharrocks, 2006). This was confirmed by increased EdU incorporation in T47D and BT20 stimulated with EGF upon pre-treatment with FGF10 (Fig 4G, Appendix Fig S5A). The use of specific inhibitors indicated that FGF10 significantly increased EGF-dependent cell cycle progression in an FGFR-, ERK-, and EGFR-dependent manner (Fig 4G and H and Appendix Fig S5).

In conclusion, FGF10 pre-treatment stabilizes EGF-stimulated EGFR via FGFR-ERK signalling. Elevated ERK phosphorylation, increased expression of ERK late target genes, and enhanced cell

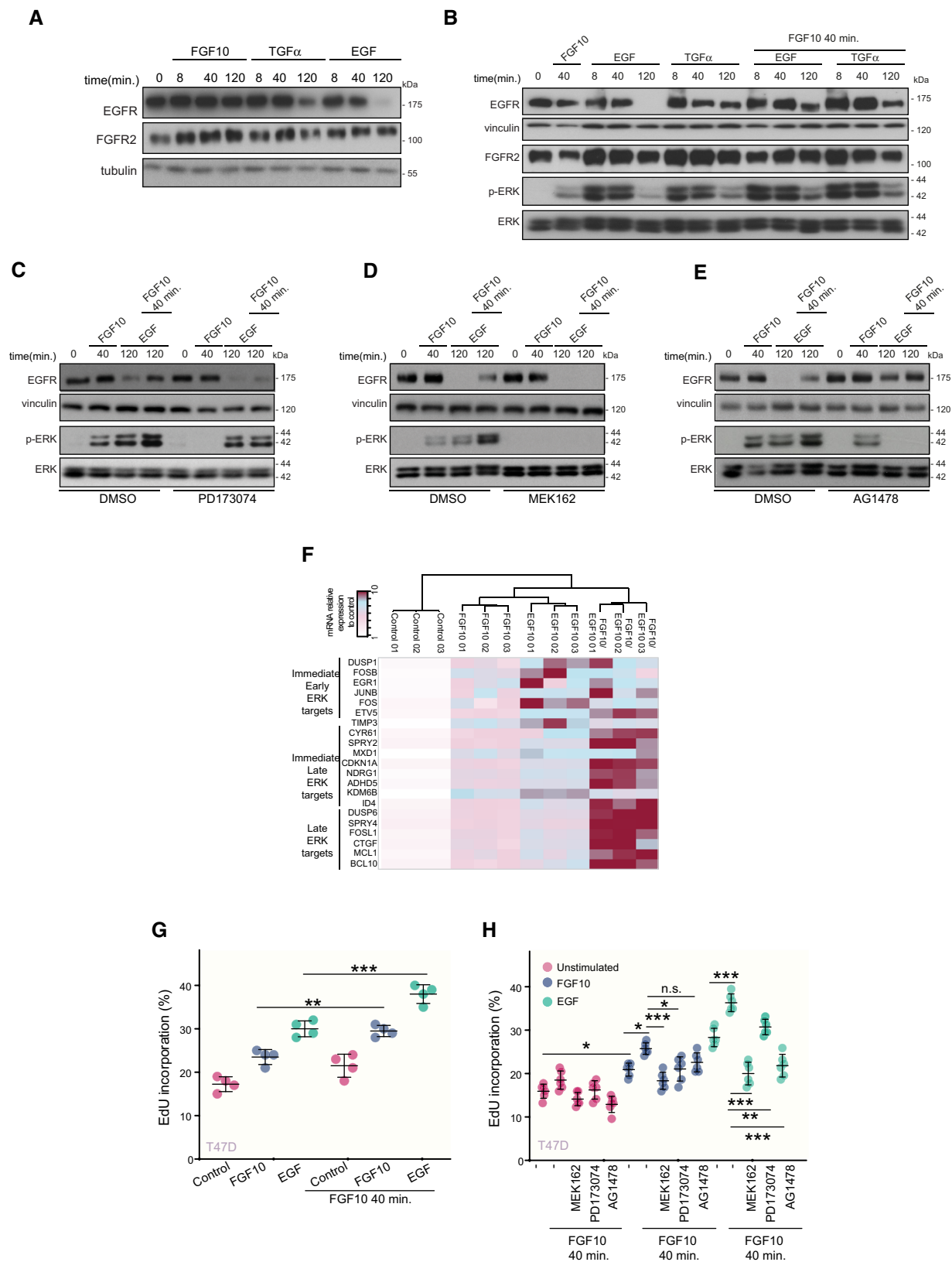


Figure 4.

Figure 4. FGF10 primes EGFR responses.

- A–E Lysates from T47D stimulated or not with FGF10, EGF or TGF α for different time periods (A); pre-treated or not with FGF10 for 40 min. and either stimulated or not with FGF10, EGF or TGF α for different time periods (B) or treated with PD173074 (C), MEK162 (D), AG1478 (E) before stimulation were immunoblotted with the indicated antibodies.
- F Heatmap of the mRNA relative expression of the indicated ERK targets compared with control and quantified by qPCR. $N = 3$. The minimum and maximum fold-induction is colour-coded in white and burgundy, respectively.
- G, H Percentage of EdU incorporation in T47D pre-treated or not with FGF10 for 40 min. and stimulated or not with FGF10 or EGF (G) or incubated with MEK162, PD173074 or AG1478 before pre-treatment (H). $N = 6$. $P = < 0.05^*$, $< 0.01^{**}$, $< 0.001^{***}$ (one-way ANOVA with Tukey test).

cycle progression suggest that FGF10 pre-treatment primes EGF responses and confirms a functional interplay between FGFR and EGFR signalling.

FGF10-dependent EGFR_T693 phosphorylation in the recycling endosome reciprocate priming of FGFR2b outputs

The FGFR/EGFR interplay was also verified by uncovering the co-localization of FGFR2b with EGFR in recycling endosomes upon 40-min. stimulation with FGF10, but not with TGF α (Fig 5A and B, Appendix Fig S6A and B). Intriguingly, EGFR was phosphorylated on T693 in recycling endosomes at 40, but not at 20 min, in response to FGF10 (Fig 5C and D, Appendix Fig S6C). We therefore hypothesized that the recycling endosomes may form the interface for FGFR and EGFR signal integration, perhaps involving physical interaction of the receptors, and that EGFR_T693 phosphorylation could affect FGFR2b trafficking. We assessed FGFR2b/EGFR co-localization and co-immunoprecipitation in T47D cells depleted of endogenous EGFR and transfected with either EGFR wild-type (wt) or the T693A mutant (T693A)—which cannot be phosphorylated at residue T693—upon a time-course stimulation with FGF10 (Fig 5, Appendix Fig S6, Appendix Fig S7A and B). Under non-stimulated conditions, FGFR2b co-localized at the plasma membrane and co-immunoprecipitated with both wt and T693A EGFR (Fig 5E–G, Appendix Fig S6D–F). At 20-min. stimulation with FGF10, FGFR2b was detected in the recycling endosomes in both wt- and T693A-expressing cells, but it failed to interact or localize with either EGFR as both were still located at the plasma membrane (Fig 5E–F, Figs EV1 and EV2, Appendix Fig S6G). Therefore, FGFR2b traffics to the recycling endosomes before interacting with EGFR. We also observed that FGFR2b localization to the recycling endosomes in FGF10 stimulated wt-expressing cells for 40 min. was lost in the presence of T693A. At this time point, FGFR2b co-immunoprecipitated with both wt and T693A (Fig 5G), but co-localized with wt in recycling endosomes and with T693A at the plasma membrane. These data imply that FGFR2b trafficking is altered in cells expressing T693A EGFR. Interestingly, RCP failed to interact with FGFR2b in T693A-expressing cells stimulated for 40 min. with FGF10 (Fig 5G, Appendix Fig S6F, suggesting that RCP and EGFR interact with FGFR2b in recycling endosomes in a T693 phosphorylation-dependent manner. Finally, at 60-min stimulation with FGF10, we detected FGFR2b and EGFR at the plasma membrane in both wt- and T693A-expressing cells (Fig 5E–G, Appendix Fig S6F–G). TGF α stimulation of T693A-expressing cells confirmed that T693 phosphorylation regulates EGFR internalization (Heisermann *et al*, 1990), as the T693A receptor was unable to traffic from the plasma membrane under any of the tested conditions (Fig 5E and F). Using GFP-Rab11-APEX2, which did not affect

FGFR2b trafficking (Appendix Fig S6H), we assessed at which time point the majority of EGFR phosphorylated on T693 was detected in proximity to the recycling endosomes following FGF10 stimulation. In agreement with the confocal imaging, we found that EGFR phosphorylation on T693 accumulated at the recycling endosomes between 20- and 40-min stimulation, when FGFR2b was detected in recycling endosomes together with RCP (Appendix Fig S6G–I, Fig 5). Altogether, these data suggest that EGFR_T693 phosphorylation dynamically regulates FGFR2b trafficking after the formation of an FGFR2b/EGFR/RCP complex in the recycling endosomes. Indeed, in T693A-expressing and in cells treated with FGFR and ERK inhibitors, but not EGFR or p38 inhibitors, there is less intracellular FGFR2b and increased receptor at the cell surface at 40-min. stimulation (Fig 5H, Appendix Fig S6J and K). Therefore, FGF10-dependent EGFR_T693 phosphorylation via FGFR and ERK activation (Fig 3) plays a role in the spatio-temporal regulation of FGFR2b trafficking.

To test the cellular impact of FGFR/EGFR signalling integration by quantifying whether EGFR_T693 phosphorylation affects FGF10 signalling downstream from FGFR2b, we compared the phosphoproteome of T47D expressing either wt or T693A EGFR upon stimulation with FGF10 for 40 or 60 min (Fig 6A, Dataset EV6). We confirmed the absence of T693 phosphorylation of T693A EGFR, whilst other EGFR residues and ERK were phosphorylated in both wt- and T693A-expressing cells (Appendix Fig S7A and B). The reproducibility of this dataset was consistent with the previous ones (Appendix Figs S1–S3, S7C–G, Datasets EV1–EV6). Hierarchical clustering of the 6485 identified phosphorylated sites revealed 4 clusters. Three clusters grouped sites whose phosphorylation increased in T693A- compared with wt-expressing cells. These clusters (plasma membrane response, acquired response, and late response) were enriched for general cellular processes (Fig 6B and C). The fourth cluster (T693 phosphorylation-dependent response) represented phosphorylated sites dependent on EGFR_T693 phosphorylation downstream from FGF10 signalling (Fig 6B and C). Of the 102 phosphorylated sites identified on the 53 kinases within all the four clusters, 10 were known regulatory sites (Fig 6D, Datasets EV6 and EV7). More specifically, FGF10-stimulated T693A-expressing cells showed decreased phosphorylation of proteins belonging to the GO term cell cycle, including the activating T161 site on the cell cycle regulator cyclin-dependent kinase 1 (CDK1) (Coulonval *et al*, 2011) (Fig 6D, Appendix Fig S7H, Dataset EV7). We confirmed that FGF10 induced CDK1_T161 phosphorylation in wt-, but not T693A-expressing T47D and BT20 cells (Fig 6E–F). Furthermore, FGF10-mediated cell cycle progression decreased in T693A-expressing cells, an effect due to impaired EGFR_T693 phosphorylation, as the total level of EGFR wt or T693A did not alter over time (Fig 7A and B, Appendix Fig S7I). Therefore, FGF10-

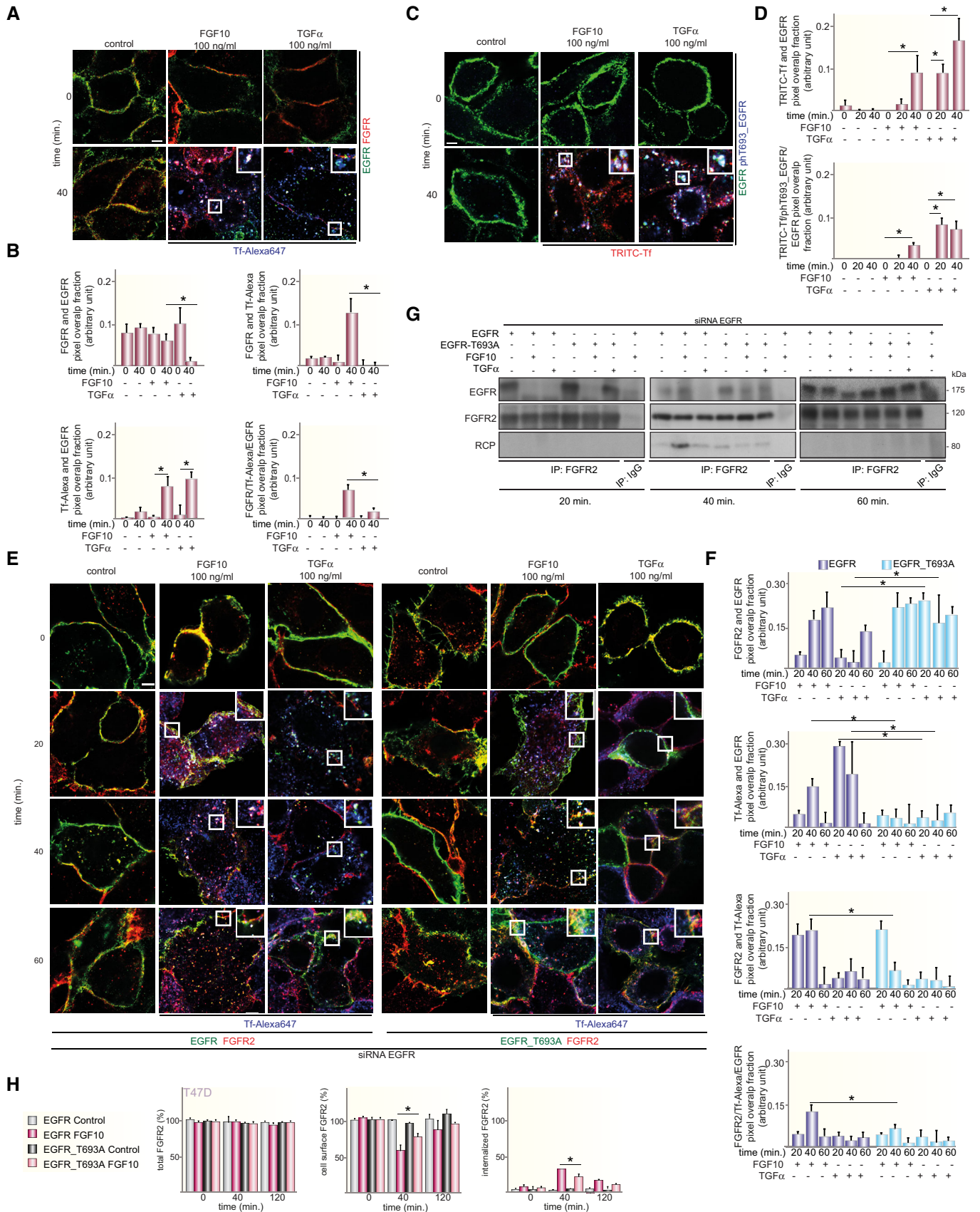


Figure 5. EGFR_T693 phosphorylation regulates FGFR2b recycling.

- A Co-localization of FGFR2 (red), EGFR (green) and the recycling marker Tf (blue) in T47D stimulated or not with FGF10 or TGF α for 40 min. Scale bar, 5 μ m.
- B Red and green pixels overlap fraction (above, left) representing the co-localization of FGFR2 with EGFR; red and far-red pixels overlap fraction (above, right) representing the co-localization of FGFR2 with the recycling marker Tf; far-red and green pixels overlap fraction (below, left) representing the co-localization of EGFR with the recycling marker Tf; green, red and far-red pixels overlap fraction (below, right) representing the co-localization of FGFR2, EGFR, and the recycling marker Tf in T47D stimulated for 40 min. Values represent the median \pm SD of at least 3 independent experiments. Representative pictures are shown in A and Appendix Fig S6A. *, P -value < 0.005 (Student's t -test).
- C Co-localization of EGFR (green), T693 phosphorylated EGFR (blue) and the recycling marker Tf (red) in T47D stimulated or not with FGF10 or TGF α for 40 min. Scale bar, 5 μ m.
- D Red and green pixels overlap fraction (above) representing the co-localization of EGFR with the recycling marker Tf; green, red and far-red pixels overlap fraction (below) representing the co-localization of EGFR, phosphorylated EGFR and the recycling marker Tf in T47D stimulated for 40 min. Values represent the median \pm SD of at least 3 independent experiments. Representative pictures are shown in C and Appendix Fig S6C. * P < 0.005 (Student's t -test).
- E Co-localization of FGFR2 (red), EGFR (green) and the recycling marker Tf (blue) in T47D depleted of EGFR by siRNA followed by transfection with wt or T693A and stimulated or not with either FGF10 or TGF α for the indicated time periods. Scale bar, 5 μ m.
- F Red and green pixels overlap fraction representing the co-localization of FGFR2 with EGFR; far-red and green pixels overlap fraction representing the co-localization of EGFR with the recycling marker Tf; red and far-red pixels overlap fraction representing the co-localization of FGFR2 with the recycling marker Tf; green, red and far-red pixels overlap fraction representing the co-localization of FGFR2, EGFR and the recycling marker Tf in cells stimulated for 20, 40 or 60 min. with FGF10 or TGF α . Values represent the median \pm SD of at least 3 independent experiments. Representative pictures are shown in E. * P < 0.005 (Student's t -test).
- G Lysates from T47D depleted of EGFR by siRNA followed by transfection with siRNA-resistant wt or T693A and stimulated or not with either FGF10 or TGF α for the indicated time periods were used for immunoprecipitation of FGFR2 and then immunoblotted with the indicated antibodies. The inputs are shown in Appendix Fig S6F.
- H The presence (total), internalization (internalized) and recycling (cell surface) of FGFR2 in T47D depleted of EGFR by siRNA followed by transfection with wt or T693A and stimulated with FGF10 for different time periods were quantified as described (Francavilla *et al*, 2016) and in the section 'Quantification of the Recycling Assay'. Briefly, we assessed approximately 100 cells per condition and expressed the results as the percentage of receptor-positive cells over total cells (corresponding to DAPI-stained nuclei) and referred to the values obtained at time zero. Values represent the median \pm SD of $N = 3$. * P < 0.005 (Student's t -test).

mediated FGFR2b recycling, CDK1 phosphorylation, and the level of cell cycle progression all depend on EGFR_T693 phosphorylation. Finally, FGF10-dependent EGFR_T693 phosphorylation plays a crucial role in FGF10 priming of EGFR responses, as shown by decreased EdU incorporation in T693A-expressing T47D and BT20 cells stimulated with FGF10 for 40 min prior to TGF α treatment (Fig 7C and D). We have previously shown that FGF10-mediated FGFR2b recycling regulates cell migration (Francavilla *et al*, 2013) and RTK recycling is known to increase cell motility (Crupi *et al*, 2020). As FGFR2b recycling was impaired in T693A-expressing cells (Fig 5), we then investigated whether EGFR_T693 phosphorylation was required for cell invasion. Surprisingly, FGF10 stimulation increased cell invasion in both wt- and T693A-expressing cells (Fig 7E and F), implying that EGFR_T693 phosphorylation is not important for FGF10-induced cell invasion. In conclusion, our data showed that recycling endosomes facilitate EGFR_T693 phosphorylation induced by FGF10 and that T693 phosphorylation is required for the full response to FGF10 and for FGF10 to prime EGF responses (Fig 7G, Fig EV3).

Overall, the "reciprocal priming" between FGFR and EGFR is a novel mechanism to coordinate the trafficking and the signalling outputs of these two RTKs in breast cancer cells.

Discussion

This study shows that FGFR activation primes EGF-mediated responses in breast cancer cells whilst inducing EGFR_T693 phosphorylation from the recycling endosomes. Such phosphorylation events in turn modify the FGFR responses. This reciprocal priming between FGFR and EGFR from the recycling endosomes alters the dynamics of recycling and enhances cell cycle progression, but not cell invasion, downstream from both RTKs. It represents the first early, selective and multi-functional mechanism of RTK signalling

integration which drives long-term outputs. In contrast to the known RTK cross-talk, where the inhibition of a dominant RTK may result in the compensatory recruitment of signalling molecules to a second RTK (Cao, 2016), reciprocal priming does not occur sequentially, rather simultaneously during the entry route of each RTK into the cytoplasm. This is an efficient way to rapidly change cell behaviour in response to the presence of a combination of ligands in the cell environment. Based on our comprehensive resource which integrates four quantitative phosphoproteomics datasets, we suggest that several recycling and signalling factors identified in this study may play a role in ensuring the co-localization of RTKs in the same cellular compartment. TPAs can be also explored by the community to pinpoint the molecular determinants of RTK recycling-dependent signalling in breast cancer cells. We therefore envision that reciprocal priming discovered in this study is unlikely to be restricted to FGFR and EGFR, opening up an exciting and novel avenue of RTK biology to be investigated. For instance, it remains to be determined whether FGFs induce the phosphorylation of threonine residues via ERK activity also on other RTKs. The discovery of a similarly phosphorylated peptide on c-Met depending on FGFRs recycling (Fig 2 C, Dataset EV4) and on other members of the EGFR family (Fig 3 E) suggests the presence of a network among RTKs in the recycling endosomes.

Besides regulating EGFR trafficking (Heisermann *et al*, 1990), T693 phosphorylation is a highly conserved residue (see response to referees in Review Process File available online) and involved in the response to stress or to the anti-tumour agent cisplatin via p38 activation (Winograd-Katz & Levitzki, 2006; Zwang & Yarden, 2006). Here, we show that FGFR ligands can induce EGFR_T693 phosphorylation and that T693 phosphorylation is required for the full activation of FGF10 responses and for FGF10 priming of EGFR outputs. This increases the repertoire of stimuli, including tumour necrosis factor- α (TNF- α) (Singhirunnusorn *et al*, 2007) or the Eph family

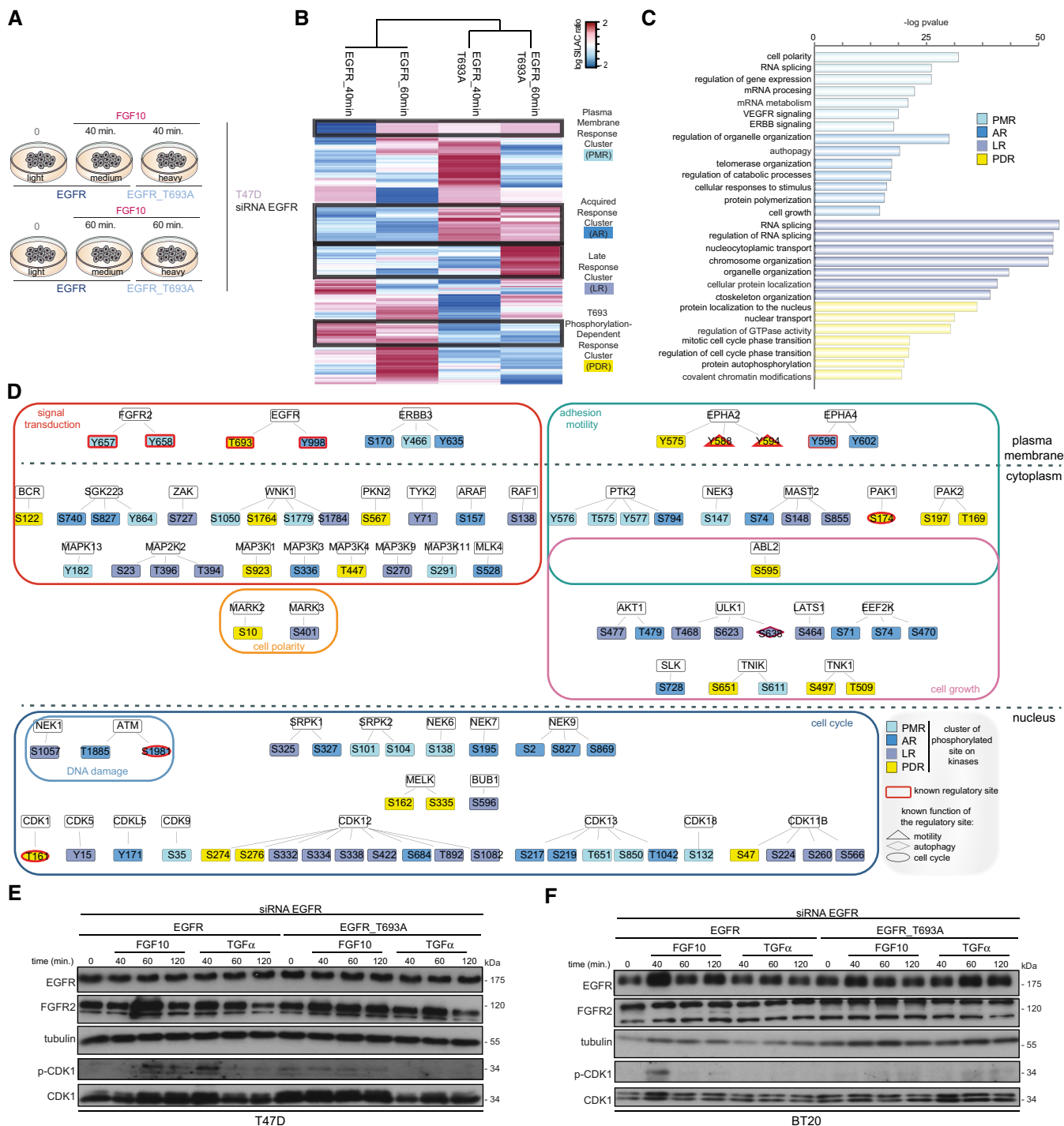


Figure 6. EGFR_T693 phosphorylation controls CDK1 phosphorylation.

- A** Experimental design of MS-based quantitative phosphoproteomics analysis of wt- and T693A-expressing T47D cells stimulated with FGF10 for 40 or 60 min.
- B** Hierarchical clustering of the phosphorylated sites differentially quantified in wt- and T693A-expressing T47D stimulated or not with FGF10 for 40 or 60 min. Four clusters for plasma membrane response (PMR), acquired response (AR), late response (LR), and T693 phosphorylation-dependent response (PDR) are highlighted with black lines and colour-coded on the right with blue, medium or dark blue and yellow, respectively. The intensity of phosphorylated sites is presented on the logarithmic scale with intensity below and above the mean colour-coded in blue and red, respectively.
- C** KEGG pathways enriched in each cluster.
- D** STRING-based and Cytoscape-visualized network of phosphorylated kinases colour-coded based on clusters shown in Fig 6C. The border of known regulatory sites is coloured in burgundy. The shape depends on the known function of the regulatory site.
- E, F** Lysates from T47D (E) and BT20 (F) depleted of EGFR, transfected with wt or T693A, and stimulated or not with either FGF10 or TGF α for the indicated time intervals were immunoblotted with the indicated antibodies.

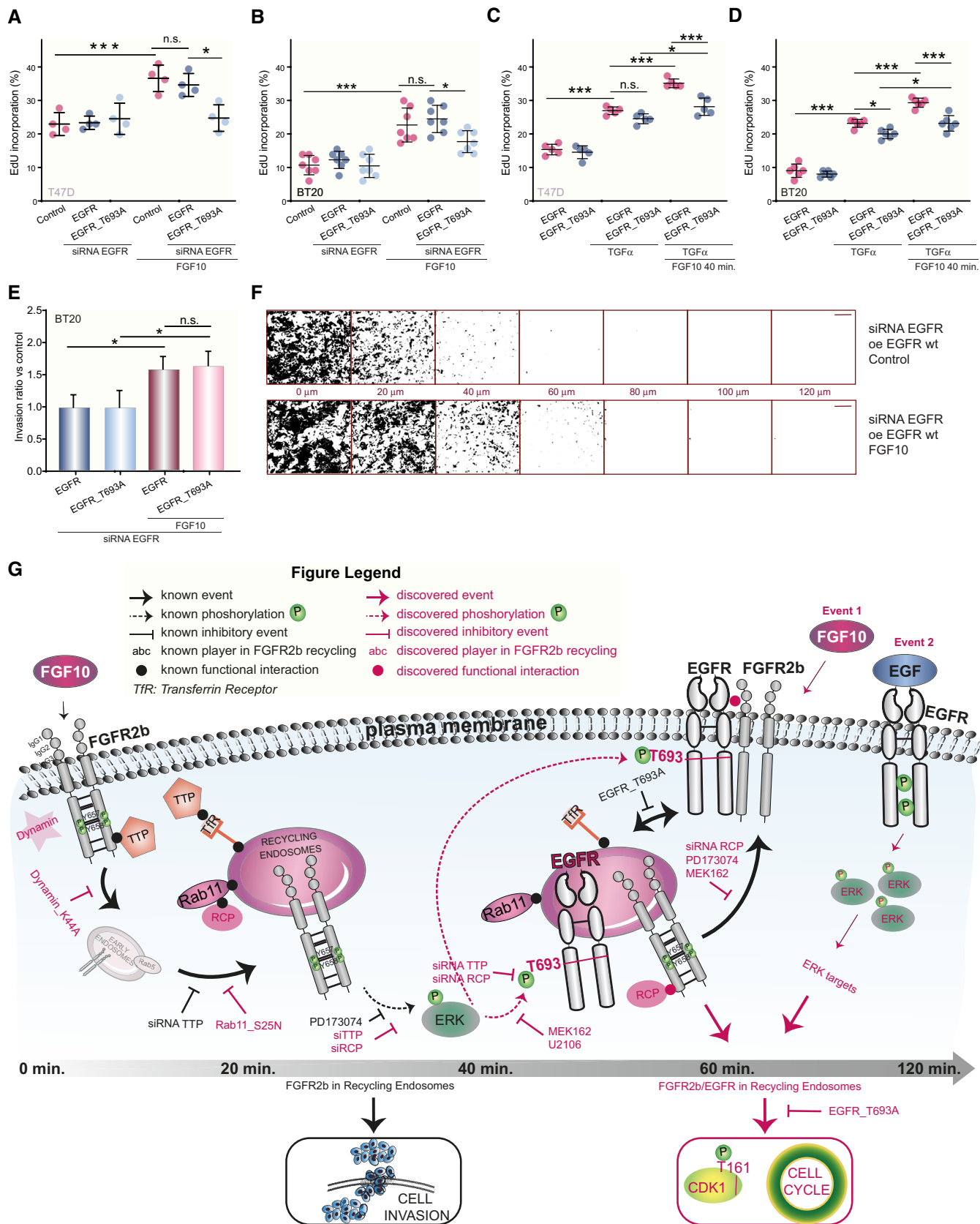


Figure 7.

Figure 7. FGF10-induced cell cycle progression depends on EGFR_T693 phosphorylation.

- A–D Percentage of EdU incorporation in T47D (A, C) or BT20 (B, D) depleted of EGFR or not, transfected with wt or T693A, and stimulated or not with FGF10 (A, B) or with TGF α (C, D) and pre-treated (C, D) or not (A, B) with FGF10 for 40 min. Values represent the median \pm SD of $N = 4$. $P < 0.05^*$, $< 0.01^{**}$, $< 0.001^{***}$ (one-way ANOVA with Tukey test).
- E Relative invasion of wt- or T693A-transfected BT20 cells into fibronectin-supplemented collagen I was quantified as described in Material and Methods. Graph depicts mean \pm SEM of $N = 8$. $*P < 0.05$ (Student's *t*-test).
- F Representative images of E. Black indicates cells. Confocal depth is indicated between panels. Scale bar, 250 μ m. oe, overexpression.
- G Model of reciprocal priming between FGFR and EGFR, based on this study.

(Stallaert *et al*, 2018), and the mechanisms which modulate EGFR activity with strong implications for RTK signalling integration. This concept is also supported by data showing that EGF-mediated phosphorylation of FGFR1 can be a route of RTK cooperation (Zakrzewska *et al*, 2013). Hence, further comprehensive studies are needed to fully understand how RTKs act in concert *in vivo* in response to the simultaneous presence of multiple ligands and how they ultimately regulate cell fate.

The dynamics of RTK trafficking is affected by several factors and in turns affects downstream signalling. For instance, EGFR recycles through recycling endosomes even in the absence of stimuli (Baumdick *et al*, 2015) and can be found in a subset of perinuclear compartments (Tomas *et al*, 2015). This potentially explains why the majority of EGFR_T693 phosphorylation is found at recycling endosomes upon FGF10 stimulation between 20 and 40 min, a time point when FGFR2b itself starts accumulating in the recycling endosomes. In turn, FGFR2b trafficking is deregulated when EGFR remains at the plasma membrane, e.g. in the absence of T693 phosphorylation, suggesting that the transient formation of the EGFR/FGFR2b complex on recycling endosomes is the key regulatory event for the correct *timing* of FGFR2b trafficking. One alternative model is that FGFR2b is internalized, traffics back to the plasma membrane where it retrieves EGFR, then reinternalizes (potentially recycling together EGFR), but the reinternalization step stalls without phosphorylation at T693. Another possibility is that FGFR2b phosphorylates the EGFR to prevent its recycling to the plasma membrane, thus explaining the change in EGFR distribution. This process should be replicated in FGF7-stimulated cells and would require further validation by high-resolution imaging of pools of FGFR2b and EGFR from the plasma membrane to recycling endosomes and back. The phosphorylation of EGFR might delay FGFR recycling back to the plasma membrane, thus allowing the formation of specific signalling complexes at the recycling endosomes. The kinases AKT and PAK1 identified by the three TPAs experiments would be interesting candidates to focus on to test this hypothesis. The alteration of the kinase landscape shown in T693A-expressing cells (Fig 6D) also confirms the idea that the EGFR phosphorylation may work as a scaffold for the recruitment of recycling machinery (e.g. RCP) and signalling partners to FGFR2b. The hypothesis of a multi-step regulation of FGFR2b—and possibly other RTKs—recycling is supported by our data on TTP and RCP. FGFR2b was not detected in recycling endosomes in TTP-depleted cells (Fig 1H); therefore, we propose that TTP is required for FGFR2b *entry* into recycling endosomes in epithelial cells (Fig 1I) (Francavilla *et al*, 2013). This would explain the lack of T693 phosphorylation and FGFR2b degradation in the absence of TTP. The third player in the complex regulation of FGFR2b recycling is RCP, which is bound to FGFR2b and EGFR in the recycling endosomes. As FGFR2b localized to recycling endosomes in RCP-depleted cells (Fig 1H), but it is partially degraded in this condition (Fig 1I), RCP may play a role in

FGFR2b *exit* from recycling endosomes. Therefore, RCP plays a temporally unique role in FGFR2b trafficking besides being a regulator of EGFR and integrin recycling (Caswell & Norman, 2008; Francavilla *et al*, 2016). We speculate on the presence of different populations of endosomes, either leading to recycling to plasma membrane (RCP-positive) or to receptor degradation (RCP-negative), implying that different families of RTKs regulate each other trafficking and signalling through a pool of adaptors on recycling endosomes. Future studies will reveal these adaptors upon different perturbations to build a more comprehensive regulatory network of RTK trafficking.

RTK recycling is known to control cellular responses, including proliferation, migration and invasion (Caswell & Norman, 2008; Francavilla *et al*, 2013; Francavilla *et al*, 2016). Here, we show that the multi-layered regulation of FGFR2b by ligand nature, trafficking route and EGFR priming fine-tunes downstream responses. Whereas cell migration and invasion require a signal from FGFR2b in recycling endosomes (Francavilla *et al*, 2013), the signal to fully promote the cell cycle occurs in a precise time window, when FGF10 primes FGFR2b and EGFR to recycling endosomes. As in the absence of the FGFR/EGFR reciprocal priming growth factors are less mitogenic but remain pro-migratory, we propose that recycling endosomes are dynamic signalling hubs that enable cells to coordinate cell cycle progression and cell invasion in response to multiple growth factors. Therefore, modulating RTK communication at early time windows might be an efficient way to re-direct cellular responses *in vivo*.

The simultaneous presence of RTKs has been described in breast cancer (Butti *et al*, 2018), where it might account for response to combined therapies (Issa *et al*, 2013), acquired resistance (Hanker *et al*, 2017) and epithelial cell-stroma communication (Wu *et al*, 2018). However, the concept of reciprocal priming has not been explored yet. It might have implications in TNBC, where both FGFRs and EGFR are highly expressed (Butti *et al*, 2018). Although we have not tested the effect of T693 phosphorylation in normal breast cells or in the stroma (Weber *et al*, 2005), this phosphorylated site may become a prognostic or predictive marker, if a correlation between T693 phosphorylation, clinical parameters and the response to combined EGFR/FGFR therapies is determined. This idea is supported by the detection of T693 phosphorylation in 50% of the TNBC patient-derived samples analysed in two independent phosphoproteomic datasets (Mertins *et al*, 2016; Huang *et al*, 2017). Importantly, reciprocal priming of RTKs may have implications when only one receptor is targeted as part of personalized therapies, where knock on effects to other pathways are not explored until resistance mechanisms have arisen (Tan *et al*, 2017). Targeting pan RTK trafficking (Porebska *et al*, 2018) and trafficking players, like TTP, RCP, and those identified by TPAs might open up novel therapeutic scenarios for treatment. Indeed, most of the recycling players identified here are mutated in breast cancer according to the

COSMIC database (Tate *et al*, 2019) and the importance of trafficking proteins in breast cancer is emerging (Wittkowski *et al*, 2018).

Understanding the extent of RTK regulation “in the right place at the right time” (Barrow-McGee & Kermorgant, 2014) is key for the integration of early signalling and long-term responses in cancer

cells. Here, we unveiled a new form of RTK communication, a reciprocal priming coordinated from the recycling endosomes. Thus, the integration of TPAs offers a wealth of new candidates to investigate the functional consequences of trafficking-mediated signalling and has the potential to guide individualized treatment in cancer and other disease (Butti *et al*, 2018; Kobayashi *et al*, 2020).

Material and Methods

Materials availability

Further information and requests for resources and reagents should be directed to and will be fulfilled by Chiara Francavilla by email at chiara.francavilla@manchester.ac.uk.

Reagents and Tools table

This information is provided in a separate Reagents and Tools Table.

Reagent or Resource	Source	Identifier
Antibodies		
Rabbit anti Phospho-EGF Receptor (Tyr1068) Antibody	Cell Signaling Technology	2234S
Mouse monoclonal Phospho-p38 MAPK (Thr180/Tyr182) (28B10)	Cell Signaling Technology	9216S
Rabbit polyclonal CDK1 (phospho T161)	Abcam	ab47329-100ug
Rabbit polyclonal CDK1	Abcam	ab131450-100ug
Mouse monoclonal FIP1/RCP antibody	Bio Techne	NBP2-20033
Mouse monoclonal ERK 1/2	Santa Cruz Biotechnology	sc-135900
Mouse monoclonal γ -Tubulin	Sigma-Aldrich	T5326
Mouse monoclonal Vinculin	Sigma Aldrich	V9264-200UL
Rabbit polyclonal pEGFR Thr669	Cell Signaling Technology	3056s
Rabbit monoclonal pEGFR Thr669	Cell Signaling Technology	8808s
Rabbit monoclonal p44/42 MAPK (Erk1/2) (137F5)	Cell Signaling Technology	4695S
Mouse monoclonal GAPDH	Abcam	ab8245-100ug
Mouse monoclonal EGFR (Ab-1)	Merck	GR01L-100UG
Rabbit polyclonal EGFR	millipore	06-847
Rabbit monoclonal FGFR1 antibody D8E4	Cell Signaling Technology	9740
Rabbit polyclonal SH3BP4	Abcam PLC	ab106609-100ug
Rabbit monoclonal FGF Receptor 2 (D4L2V)	Cell Signaling Technology	23328S
Rabbit monoclonal P38	Cell Signaling Technology	9212
Rabbit monoclonal GFP	Cell Signaling Technology	2956
Peroxidase-AffiniPure F(ab') ₂ Fragment Goat Anti-Mouse IgG (H + L) (min X Hu, Bov, Hrs Sr Prot)	Stratech	115-036-062-JIR-0.5ml
Peroxidase-AffiniPure F(ab') ₂ Fragment Goat Anti-Rabbit IgG (H + L) (min X Hu Sr Prot)	Stratech	111-036-045-JIR-0.5m
Mouse monoclonal to EEA1	BD Bioscience	610457
Goat anti-Rabbit IgG (H + L) Secondary Antibody, Alexa Fluor [®] 488 conjugate	Invitrogen	A11034
Goat anti-Mouse IgG (H + L) Secondary Antibody, Alexa Fluor [®] 488 conjugate	Invitrogen	A11001
Goat anti-Rabbit IgG (H + L) Secondary Antibody, Alexa Fluor [®] 568 conjugate	Invitrogen	A11011
Donkey Anti-Mouse IgG (H + L) Secondary Antibody, Alexa Fluor [®] 647 conjugate	Invitrogen	A31571
Donkey Anti-Rabbit IgG (H + L) Secondary Antibody, Alexa Fluor [®] 647 conjugate	Invitrogen	A31573

Reagents and Tools table (continued)

Reagent or Resource	Source	Identifier
Bacterial and Virus Strains		
NEB® 10-beta Competent E. coli (High Efficiency)	New England Biolabs	Cat. No: C3019H
Biological Samples		
Chemicals, Peptides, and Recombinant Proteins		
Trypsin porcine pancreas (proteomics grade)	Sigma-Aldrich	T6567
Lysyl Endopeptidase	FUJIFILM Wako Chemicals	2541
TiO beads "Titanspheres"	GL Sciences	5020-75000
Pre-cast gradient gel: Nu-PAGE 4-12% Bis-Tris Gel 1.0mm 10 well	Invitrogen	NP0321BOX
Sep-Pak Classic C18 cartridges	Waters	WAT051910
Solid Phase Extraction Disk "Empore" C18 (Octadecyl) 3 M	Agilent Technologies	2215
Solid Phase Extraction Disk "Empore" C8 (Octyl) 3 M	Agilent Technologies	2214
L-ARGININE:HCL	Cambridge Isotope Laboratories	CLM-2265-H-0.25
L-ARGININE:HCL	Cambridge Isotope Laboratories	CNLM-539-H-0.5
L-ARGININE:HCL	Sigma-Aldrich	A6969
L-LYSINE:2HCL	Cambridge Isotope Laboratories	DLM-2640-0.5
L-LYSINE:2HCL	Cambridge Isotope Laboratories	CNLM-291-H-0.5
L-LYSINE:2HCL	Sigma-Aldrich	L8662
2,5-Dihydroxybenzoic acid	Sigma-Aldrich	85707
RPMI 1640 Medium for SILAC	ThermoFisher Scientific	88365
TRIZOL™ Reagent	ThermoFisher Scientific	Cat. No. 15596026
DIHYDROETHIDIUM	Cambridge Bioscience	12013-5mg-CAY
Hoechst 33342	New England Biolabs	4082S
Lipofectamine RNAiMAX Transfection Reagent	ThermoFisher Scientific	10601435
Lipofectamine Transfection Reagent	Life Technologies	18324020
FuGENE HD Transfection Reagent	Promega UK	E2311
Sodium Pyruvate solution 100mM (100ml)	Sigma-Aldrich	S8636-100ML
Crystal violet solution	Sigma-Aldrich	V5265-250ML
Carestream Kodak BioMax MR Film	Kodak	Z350370-50EA
Xtra-Clear Flat 8-Strip Caps	Star labs	I1400-0900-C
96-Well PCR Plate Non-Skirted Low Profile Natural	Star labs	E1403-0200-C
RPMI 1640 Medium Glutamax Supplement (500ml)	Gibco	61870010
ReliaPrep RNA Cell Miniprep System	NEB	Z6011
Color Prestained Protein Standard Broad Range	NEB	P7712S
Prestained Protein Standard Broad Range	Sigma-Aldrich	SDS7B2
PURELINK QUICK MINI	NEB?	K210010
T4 DNA Ligase 20,000 u	NEB?	M0202S
DMEM High glucose HEPES w/o Glutamine and Sodium pyruvate	Sigma-Aldrich	D6171-6X500ML
DMEM AQ medium	Sigma-Aldrich	D0819-500ml
RPMI 1640 w/L-Glutamine-Bicarbonate	Sigma-Aldrich	R8758-6X500ML
Q5 High Fidelity 2x mastermix	NEB	M0492S
Nutrient Mix F12 HAM	Sigma-Aldrich	N6658-500ML
Human EGF (Animal Free)	PeproTech	AF-100-15-1000
PRESTAINED MOLECULAR WEIGHT MARKER, MW 2	Sigma-Aldrich	SDS7B2-1VL
MG132	Fisher Scientific	15465519
HYPERFILM ECL 18X24CM	VWR International Ltd	28-9068-37

Reagents and Tools table (continued)

Reagent or Resource	Source	Identifier
Albumin, Bovine Fraction V (BSA), 100 Grams Cat No: A30075-100.0	Melford Biolaboratories Ltd	A30075-100.0
Bradford Reagent	Bio-Rad	5000205
Clarity ECL	Bio-Rad	1705061
GoScript Reverse Transcription Mix, Random Primers	Promega	A2801
Pierce Protease Inhibitor Tablets-20 tablets	Life Tehnologies	A32963
MEMBRANE PROTRAN 0,45uM NC 300MMX4 M	VWR	10600002
qPCRBIO SyGreen Mix Separate-ROX	pcr biosystems	PB20.14-50
ProLong Diamond Antifade Mountant-2 mL	Life Technologies	P36965
ExoSAP-IT	Life Technologies	78250.40.ul
DMSO	Sigma-Aldrich	276855-250ml
ACETONITRILE	VWR International Ltd	1.00030.2500
HEPARIN SODIUM CELL CULTURE TESTED	Sigma-Aldrich	H3149-100KU
Escort IV	SLS	L3287-1ML
Penicillin-Streptomycin (10,000 U/ml)	Life Technologies Ltd	15140122
Human EGF	Sigma-Aldrich	E9644-2MG
Human TGF α	Pepto Tech Limited	100-16A
Human FGF1	Pepto Tech Limited	100-17A-50
Human FGF7	Francavilla <i>et al</i> 2013	PI: Prof Olsen
Human FGF3	Bio Techne	1206-F3-025
Human FGF10	Francavilla <i>et al</i> 2013	PI: Prof Olsen
Enkamin-E	Pepto Tech Limited	A14-529EP
PD173074	Selleckchem	S1264
AG1478	Cell Signalling Technologies	9842
U2106	Cell Signalling Technologies	9903
MEK162	APEXBIO	A1947
BMS582949	Selleck Chem	S8124
Collagen I, HC, Rat Tail, 100 mg	Corning	354249
FIBRONECTIN FROM BOVINE PLASMA	Sigma	F1141-1MG
DMEM powder, high glucose	Thermo Fisher	52100021
Fetal Bovine Serum, South American origin	Life Technologies	10270106
TW PC MEMBRANE,6,5MM,8,0UM Transwell Inserts	Sigma Aldrich	CLS3422-48EA
Calcein AM cell permanent Dye	Fisher Scientific	C1430
Glacial Acetic Acid (HPLC Grade)	Fisher Scientific UK	10060000
Formic Acid (HPLC Grade)	Sigma-Aldrich	5438040250
Trifluoroacetic Acid (Spectroscopy Grade)	Sigma-Aldrich	1082621000
Dispase	Stem Cell Technologies	7913
Matrigel	Corning	354230
DAPI (4',6-Diamidino-2-Phenylindole, Dihydrochloride)	Life Technology	D1306
Transferrin From Human Serum, Alexa Fluor™ 647 Conjugate	Invitrogen	T23366
Transferrin From Human Serum, Tetramethylrhodamine Conjugate	Invitrogen	T2872
Critical Commercial Assays		
Click-iT Edu Alexa Fluor 488 Imaging Kit-1 kit	Life Technologies	C10337
Venor®GeM Classic Mycoplasma PCR Detection Kit(100 tests)	Cambridge Bioscience	11-1100
ProtoScript; II First Strand cDNA Synthesis Kit	New England Biolabs	E6560L
ReliaPrep RNA Cell Miniprep System	Promega	Z6011

Reagents and Tools table (continued)

Reagent or Resource	Source	Identifier
Tumor dissociation kit	Miltenyi Biotec	130-095-929
Isolate II PCR and Gel kit	Bioline	BIO-52059
Isolate II plasmid mini kit	Bioline	BIO-52056
Deposited Data		
Raw data (MS)	This paper	http://proteomecentral.proteomexchange.org/cgi/GetDataset (dataset identifier PXD018184)
Experimental Models: Cell Lines		
MCF-7	LGC ATCC®	HTB-22
MDA-MB-415	LGC ATCC®	HTB-24
BT20	LGC ATCC®	HTB-19
HCC1937	LGC ATCC®	CRL-2336
T47D	LGC ATCC®	HTB-133
BT549	LGC ATCC®	HTB-122
Experimental Models: Organisms/Strains		
BB6RC37	Eyre <i>et al</i> (2016)	PI: R. Clarke
Oligonucleotides		
SIRNA UNIV NEGATIVE CONTROL #2	Sigma-Aldrich	SIC002
GGAGAUGAAAGUGUCAGCCGAGUAU	Invitrogen	SH3BP4HSS119149
CCCAGGAUCUCAAGGUCUGUAUGUU	Invitrogen	SH3BP4HSS119150
CCUGAUUGACCCUGAGCGAAGGGUUU	Invitrogen	SH3BP4HSS119151
GGUCCUCAAACAGAAGGAAACGAUA	Invitrogen	RAB11FIP1HSS149439
GAAGACUACAUUGACAACCGCUUG	Invitrogen	RAB11FIP1HSS149440
UCCGCAUCCCGACUCAGGUUGGCAA	Invitrogen	RAB11FIP1HSS149441
CGGAUAGGUUUGGUGAAUUUAAA	Invitrogen	EGFRHSS176346 (G01)
CCUUGCCUJAGCAGUCUUAUCUAA	Invitrogen	EGFRHSS103116 (G06)
CCCGUAAUUAUGUGGUGACAGAUCA	Invitrogen	EGFRHSS103114 (G09)
CCN1 F- GGTCAAAGTTACCGGGCAGT R- GGAGGCATCGAATCCCAGC	In house	n/a
DUSP1 F- GCCTTGCTTACCTTATGAGGAC R- GGGAGAGATGATGCTTCGCC	In house	n/a
FOS F- AGGAGGGAGCTGACTGATACACT R- TTTCTTCTCCTTCAGCAGTT	In house	n/a
JUNB F- ACGACTCATACAGCTACGG R- GCTCGGTTTCAGGAGTTTGTAGT	In house	n/a
TIMP3 F- CATGTGCAGTACATCCATACGG R- CATCATAGACCGACCTGTCA	In house	n/a
EGR1 F- GAGAAGGTGCTGGTGAGAC R- CACAAGGTGTTGCCACTGTT	In house	n/a
BCL10 F- GTGAAGAAGGACGCCTTAGAAA R- TCAACAAGGGTGCCAGACCT	In house	n/a
CTGF F- CAGCATGGACGTTCTGTCTG R- AACCAAGGTTTGGTCCTTGG	In house	n/a
MCL1 F- ATCTCTCGGTACCTTCGGGAGC R- GCTGAAAACATGGATCATCACTCG	In house	n/a
DUSP6 F- CCGCAGGAGCTATACGAGTC R- CGTAGAGCACCCTGTGTCTG	In house	n/a
ABHD5 F- GCTGCTGCTTACTCGTGAA R- TCTGATCCAAACTGGAATTGGTC	In house	n/a
KDM6B F- CACCCAGCAAACCATATTATGC R- CACACAGCCATGCAGGGATT	In house	n/a
MXD1 F- CGTGGAGAGCAGGACTATC R- CCAAGACACGCCTTGTGACT	In house	n/a
NDRG1 F- CTCCTGCAAGAGTTTGTATGTC - R- TCATGCCGATGTCATGGTAGG	In house	n/a
SPRY2 F- CCTACTGTCGTCACAGACCT R- GGGGCTCGTGCAAGAAT	In house	n/a
ID4 F- TGCCTGCAGTGCATATGAA R- GCAGGTCAGGATGTAGTCG	In house	n/a
FGFR2b F- AACGGGAAGGAGTTTAAAGCAG R- CTCGGTCACATTGAACAGAG	In house	n/a
BETA ACTIN F- TGGAACGGTGAAGGTGACAG R- AACCAACGCATCTCATATTTGGAA	In house	n/a
GAPDH F- CAATGACCCCTTCATTGACC R- GACAAGCTTCCCGTTCTCAG	In house	n/a

Reagents and Tools table (continued)

Reagent or Resource	Source	Identifier
Recombinant DNA		
EGFR (pRK5-EGFR)	Addgene	Plasmid #65225
EGFRT693A	Mutagenesis of above	
eGFP-Rab11	Addgene	Plasmid #12674
eGFP-Rab11_S52N	Mutagenesis of above	
Dynamin_K44a-eGFP	Mutagenesis of Addgene plasmid	Plasmid # 34680
HA-FGFR1c	Francavilla et al (2009)	PI: Dr Cavallaro
HA-FGFR2b	Francavilla et al (2013)	PI: Prof Olsen
HA_FGFR2b_Y656F/Y657F	Francavilla et al (2013)	PI: Prof Olsen
HA-FGFR4 cloned using human cDNA with primers F- GGGGCCAGCCGCCAGACTGGAGGCCTCTGAGGAAGTGGAGCTTGAGCC R - GTCGACCTGCAGTGTCTGCACCCAGACCCGAAGGGGAAGGAGCTGGATCC	Generated for this study	n/a
Software and Algorithms		
Fiji- Image J version: 1.52p	Schindelin et al (2012)	https://imagej.net/Fiji
GraphPad Prism version 8.0.0	GraphPad Software	www.graphpad.com
MaxQuant version 1.5.6.5	Cox and Mann (2008)	http://www.coxdocs.org/doku.php?id=maxquant:start
WebGestalt 2019	Liao et al (2019)	http://www.webgestalt.org/
Perseus versions 1.6.5.0 or 1.6.2.1.:	Tyanova et al (2016)	http://www.coxdocs.org/doku.php?id=maxquant:start
Cytoscape version 3.7.2	Shannon et al (2003)	https://www.cytoscape.org
STRING version 11	Szkarczyk et al (2019)	https://string-db.org/
R framework	R Core Team (2018)	https://www.r-project.org/
Other		
Confocal Microscope Leica Sp8 Inverted	Leica	
Mx3000P qPCR machine	Agilent	
UltiMate [®] 3000 Rapid Separation LC	Dionex	
QE-HF LC-MS/MS	Thermo Fisher Scientific	

Methods and Protocols

Experimental models

Cell culture and SILAC labelling

Human breast cancer cell lines were purchased from ATCC, authenticated through short tandem repeat (STA) analysis of 21 markers by Eurofins Genomics, checked monthly for mycoplasma via a PCR-based detection assay (Venor[®]GeM—Cambio) and grown in the indicated media supplemented with 2 mM L-glutamine and 100 U/ml penicillin, 100 µg/ml streptomycin, and 10% foetal bovine serum. MCF-7 was grown in DMEM/F12. MDA-MB-415 and BT20 were grown in DMEM. HCC1937, T47D and BT549 were grown in RPMI. 1 mM sodium pyruvate was added to T47D.

For quantitative mass spectrometry, BT549 or T47D cells were labelled in SILAC RPMI (PAA Laboratories GmbH, Germany) supplemented with 10% dialyzed foetal bovine serum (Sigma), 2 mM glutamine (Gibco), 100 U/ml penicillin and 100 µg/ml streptomycin for 15 days to ensure complete incorporation of amino acids, which was verified by MS analysis. Three cell populations were obtained: one labelled with natural variants of the amino acids (light label; Lys0, Arg0), the second one with medium variants of

amino acids (medium label; L-[13C6] Arg (+6) and L-[2H4]Lys (+4); Lys4/Arg6) and the third one with heavy variants of the amino acids (heavy label; L-[13C6,15N4]Arg (+10) and L-[13C6,15N2]Lys (+8); Lys8/Arg10). The light amino acids were from Sigma, whilst their medium and heavy variants were from Cambridge Isotope Labs (Massachusetts, US).

Breast cancer organoid culture and protein isolation

Organoids were generated from a triple-negative breast cancer PDX tumour, BB6RC37 (Eyre et al, 2016). The tumours were minced and digested using a tumour dissociation kit (Miltenyi Biotec) on an orbital shaker at 37°C for 1–2 h. The cells were sequentially strained through 100-µm and 40-µm meshes. 50,000 cells were resuspended in 50 µl cold growth factor-reduced Matrigel (Corning 354230), set as domes in a 24-well plate for 30 min and cultured at 37°C in media as defined by (Sachs et al, 2018). The organoids were cultured in media with or without FGF7/10 for 14 days, and EGF/Heregulin were removed from the media 24 h before lysates were obtained. Lysates were prepared by mechanically disaggregating the domes and digesting the Matrigel for 1 h using dispase at 37°C (Stem Cell Technologies, 7913). Cells were washed in PBS and

resuspended in lysis buffer as previously described (Santiago-Gomez *et al.*, 2019).

Quantitative phosphoproteomics

Experimental design and sample preparation

TPA1: for each cell line and each stimulus, we analysed duplicates for each time point, considering both 1- and 8-min. time points as representative of early signalling. Therefore, we compared four label-free samples for each stimulus in each cell line (Datasets EV1 and EV2). The cell pellet was dissolved in denaturation buffer (6 M urea, 2 M thiourea in 10 mM HEPES pH 8). We obtained 1 mg of proteins from each sample. Cysteines were reduced with 1 mM dithiothreitol (DTT) and alkylated with 5.5 mM chloroacetamide (CAA). Proteins were digested with endoproteinase Lys-C (Wako, Osaka, Japan) and sequencing grade modified trypsin (modified sequencing grade, Sigma) followed by quenching with 1% trifluoroacetic acid (TFA). Peptides were purified using reversed-phase Sep-Pak C18 cartridges (Waters, Milford, MA) and eluted with 50% acetonitrile (ACN). After removing ACN by vacuum concentrator at 60°C, peptides were suspended in phosphopeptide immunoprecipitation buffer (50 mM MOPS pH 7.2, 10 mM sodium phosphate, 50 mM NaCl) and dissolved overnight. Clarified peptides were transferred in a new tube containing immobilized phosphorylated tyrosine antibody beads (pY100-AC, Cell Signalling Technologies) and incubated for two hours at 4°C. After five washes with immunoprecipitation buffer followed by two washes with 50 mM NaCl, the enriched peptides were eluted from the beads three times with 50 μ L of 0.1% TFA, loaded on C18 STAGE-tips, and eluted from STAGE-tips with 20 μ L of 40% ACN followed by 10 μ L 60% ACN and reduced to 5 μ L by SpeedVac and 5 μ L 0.1% formic acid (FA) 5% ACN added. Peptides from the supernatant were purified using reversed-phase Sep-Pak C18 cartridges (Waters, Milford, MA) and eluted with 50% ACN and further enriched for phosphorylated serine- and phosphorylated threonine-containing peptides, with Titansphere chromatography. Six mL of 12% TFA in ACN was added to the eluted peptides and subsequently enriched with TiO₂ beads (5 μ m, GL Sciences Inc., Tokyo, Japan). The beads were suspended in 20 mg/mL 2,5-dihydroxybenzoic acid (DHB), 80% ACN, and 6% TFA and the samples were incubated in a sample to bead ratio of 1:2 (w/w) in batch mode for 15 min with rotation. After 5-min centrifugation, the supernatant were collected and incubated a second time with a twofold dilution of the previous bead suspension. The beads were washed with 10% ACN, 6% TFA followed by 40% ACN, 6% TFA and collected on C8 STAGE-tips and finally washed by 80% ACN, 6% TFA. Elution of phosphorylated peptides was done with 20 μ L 5% NH₃ followed by 20 μ L 10% NH₃ in 25% ACN, which were evaporated to a final volume of 5 μ L in a speed vacuum. The concentrated phosphorylated peptides were acidified with addition of 20 μ L 0.1% TFA, 5% ACN and loaded on C18 STAGE-tips. Peptides were eluted from STAGE-tips with 20 μ L of 40% ACN followed by 10 μ L 60% ACN and ACN and reduced to 5 μ L by SpeedVac and 5 μ L 0.1% FA, 5% ACN added.

A small amount of the eluted peptides (1%) was taken for proteome analysis before enrichment of phosphorylated peptides: after evaporation in a speed vacuum, 40 μ L of 0.1% TFA, 5% ACN were added followed by MS analysis.

TPA2: we analysed label-free triplicates for each condition, T47D depleted or not of TTP or RCP and stimulated or not with FGF10. Cells were washed with PBS and lysed at 4°C in ice-cold 1% triton lysis buffer supplemented with Pierce protease inhibitor tablet (Life Technologies) and phosphatase inhibitors: 5 nM Na₃VO₄, 5 mM NaF and 5 mM β -glycerophosphate. Proteins were precipitated overnight at -20°C in fourfold excess of ice-cold acetone. The acetone-precipitated proteins were solubilized in denaturation buffer (10 mM HEPES, pH 8.0, 6 M urea, 2 M thiourea), and 5 mg of proteins was reduced, alkylated and digested, as described above. All the steps were performed at room temperature. The peptide mixture was desalted and concentrated on a C18-Sep-Pak cartridge, eluted and enriched with TiO₂ beads, as described above.

TPA3: we analysed duplicates of SILAC-labelled BT549, transfected and treated as described in Fig 2A. We followed the same procedure described for TPA2 with the only difference that 5 mg of each SILAC-labelled lysates was mixed in equal amount before digestion and TiO₂ chromatography.

EGFR- and EGFR_T693A-expressing T47D cells: we analysed duplicates of SILAC-labelled T47D transfected and treated as described in Fig 6A. We followed the same procedure described for TPA1 with the only difference that 5 mg of each SILAC-labelled lysates was mixed in equal amounts before digestion and phosphorylated tyrosine enrichment followed by TiO₂ chromatography and peptides purification.

Mass spectrometry

Purified peptides were analysed by LC-MS/MS using an UltiMate[®] 3000 Rapid Separation LC (RSLC, Dionex Corporation, Sunnyvale, CA) coupled to a QE-HF (Thermo Fisher Scientific, Waltham, MA) mass spectrometer. Mobile phase A was 0.1% FA in water, and mobile phase B was 0.1% FA in ACN and the column was a 75 mm x 250 μ m inner diameter 1.7 μ m CSH C18, analytical column (Waters). A 1 μ L aliquot of the sample (for proteome analysis) or a 3 μ L aliquot was transferred to a 5 μ L loop and loaded on to the column at a flow of 300 nL/min at 5% B for 5 and 13 min, respectively. The loop was then taken out of line and the flow was reduced from 300 nL/min to 200 nL/min in 1 min., and to 7% B. Peptides were separated using a gradient that went from 7% to 18% B in 64 min., then from 18% to 27% B in 8 min. and finally from 27% B to 60% B in 1 min. The column was washed at 60% B for 3 min. and then re-equilibrated for a further 6.5 min. At 85 min, the flow was increased to 300 nL/min until the end of the run at 90 min. Mass spectrometry data were acquired in a data directed manner for 90 min in positive mode. Peptides were selected for fragmentation automatically by data-dependent analysis on a basis of the top 8 (phosphoproteome analysis) or top 12 (proteome analysis) with m/z between 300 and 1750 Th and a charge state of 2, 3 or 4 with a dynamic exclusion set at 15 s. The MS resolution was set at 120,000 with an AGC target of 3e6 and a maximum fill time set at 20 ms. The MS2 resolution was set to 60,000, with an AGC target of 2e5, and a maximum fill time of 110 ms for Top12 methods, and 30,000, with an AGC target of 2e5, and a maximum fill time of 45 ms for Top8 analysis. The isolation window was of 1.3 Th (2.6 Th for SILAC-labelled samples), and the collision energy was of 28.

Raw files analysis

Raw data were analysed by the MaxQuant software suite (Cox & Mann, 2008) (<https://www.maxquant.org>; version 1.5.6.5) using the integrated Andromeda search engine (Cox *et al*, 2011). Proteins were identified by searching the HCD-MS/MS peak lists against a target/decoy version of the human UniProt Knowledgebase database that consisted of the complete proteome sets and isoforms (v.2016; https://uniprot.org/proteomes/UP000005640_9606) supplemented with commonly observed contaminants such as porcine trypsin and bovine serum proteins. Tandem mass spectra were initially matched with a mass tolerance of 7 ppm on precursor masses and 0.02 Da or 20 ppm for fragment ions. Cysteine carbamidomethylation was searched as a fixed modification. Protein N-acetylation, N-pyroglutamine, oxidized methionine and phosphorylation of serine, threonine and tyrosine were searched as variable modifications. Protein N-acetylation, oxidized methionine and deamidation of asparagine and glutamine were searched as variable modifications for the proteome experiments. For the quantification of SILAC-labelled samples, labelled lysine and arginine were specified as fixed or variable modification, depending on prior knowledge about the parent ion (MaxQuant SILAC triplet identification). In all the other experiments, label-free parameters were used as described (Cox *et al*, 2014). False discovery rate was set to 0.01 for peptides, proteins and modification sites. Minimal peptide length was six amino acids. Site localization probabilities were calculated by MaxQuant using the PTM scoring algorithm (Olsen *et al*, 2006). The datasets were filtered by posterior error probability to achieve a false discovery rate below 1% for peptides, proteins and modification sites. Only peptides with Andromeda score > 40 were included.

Data and statistical analysis

All statistical and bioinformatics analyses were done using the freely available software Perseus, version 1.6.5.0 or 1.6.2.1. (Tyanova & Cox, 2018), R framework (R Core Team, 2018), Bioconductor R-package LIMMA (Bolstad *et al*, 2003), WebGestalt (Liao *et al*, 2019), STRING (Szklarczyk *et al*, 2019), Cytoscape (version 3.7.2) (Shannon *et al*, 2003). All measured peptide intensities were normalized using the “normalizeQuantiles” function from the Bioconductor R-package LIMMA, which normalizes the peptide intensities such that each quantile for each sample is set to the mean of that quantile across the dataset, resulting in peptide intensity distributions that are empirically identical. Each dataset was normalized individually. Subsequent data analysis was performed using Microsoft Office Excel, R and Perseus. For the SILAC datasets, we used the normalized SILAC ratios from MaxQuant output txt files. Only peptides with localization probabilities higher than 0.75 (class I, shown in Datasets EV1, EV3–EV6; Olsen *et al*, 2006) were included in the downstream bioinformatics analysis. Pearson correlation was calculated in R. For TPA1, we impute missing values using Perseus default settings, we subtracted the control from log intensity values in order to be able to compare all the cell lines against each other and we used the median for each condition. Hierarchical clustering based on correlation was performed after multi-sample ANOVA test with default parameters in Perseus. For TPA2, we calculated the median and then considered only rows with four valid values, followed by hierarchical clustering based on Euclidean distance in Perseus. For TPA3 and the EGFR/EGFR_T693A T47D dataset, we imputed missing values using Perseus default settings and then

calculated the median, followed by hierarchical clustering based on Euclidean distance in Perseus. Clusters used in the follow-up analysis were defined by Perseus and manually checked.

The enrichment of KEGG or GO terms was performed in WebGestalt using the ORA default parameters, and significantly over-represented terms within the data were represented in bar plots. The relation of genes to other diseases was based on the database DISEASES (Pletscher-Frankild *et al*, 2015).

All the protein interaction networks were obtained using the STRING protein interaction database using high confidence, and interactions derived from the Experiments and Databases evidence channels. Data visualization was performed using the software Cytoscape. The Venn diagram was created using the web tool http://bioinformatics.psb.ugent.be/cgi-bin/liste/Venn/calculate_venn.html.

Biochemical assays

RNA isolation and real-time PCR analysis

RNA from cell lines was isolated with TRIZOL[®] (Invitrogen). After chloroform extraction and centrifugation, 5 µg RNA was DNase treated using RNase-Free DNase Set (Qiagen) and 1 µg of DNase treated RNA was then taken for cDNA synthesis using the ProtoScript I first strand cDNA synthesis kit (New England Biolabs). Selected genes were amplified by quantitative real-time PCR (RT-qPCR) using Sygreen (PCR Biosystems). Relative expression was calculated using the delta-delta CT methodology, and beta-actin was used as reference housekeeping gene. Sequences for primers used can be found in the accompanying Reagent Table. qPCR machine used was Applied Biosystems MX300P.

Transfection and RNA interference

All transfections were carried out in Gibco opti-MEM glutamax reduced serum media (Thermo Fisher Scientific). For RNA interference, all cells were transfected using Lipofectamine RNAiMax (Thermo Fisher Scientific), according to manufacturer instructions. Validated double-stranded stealth siRNA oligonucleotides were used for RNA interference. siRNA Universal Negative Control #2 (Sigma-Aldrich) was used as a control in all RNA interference experiments. BT549 and BT20 cells were transfected using Lipofectamine 3000 (Thermo Fisher Scientific) according to the manufacturer's instructions, 24 h after RNA interference transfection where indicated. T47D cells were transfected using Escort IV according to manufacturer instructions, same as above. Assays were performed 36 h after transfection, as previously described (Francavilla *et al*, 2016). Where assays were performed more than 36 h after transfection, RNAi and expression were assessed at time of assay to confirm expression.

Cell lysis, protein immunoprecipitation and western blotting

Cells were serum starved overnight in serum-free medium and stimulated for the indicated time points with 100 ng/ml of FGF7, FGF10, EGF or TGF α . Ligands were replenished every 24 h for long-term (24–72 h) stimulation. Where indicated, cells were pre-incubated for 2 h with 100 nM PD173074, 500 nM AG1478, 20 µM U1206, 1 µM MEK162 or 10 µM BMS582949. Control cells were pre-incubated with DMSO alone. After stimulation, cell extraction and immunoblotting were performed as previously described (Francavilla *et al*, 2016). Proteins were resolved by SDS-PAGE and transferred to nitrocellulose membranes (Protran, Biosciences). Proteins of interest were visualized using specific antibodies, followed by

peroxidase-conjugated secondary antibodies and by an enhanced chemiluminescence kit (Amersham Biosciences). Blots were visualized either using film exposure or the Universal Hood II Gel Molecular Imaging System (Bio-Rad). Each experiment was repeated at least three times and produced similar results.

Immunoprecipitation of FGFR2 from cell extracts was performed as previously described (Francavilla *et al*, 2016), using anti BEK (Santa Cruz Biotechnology, sc-121). Each experiment was repeated at least three times and produced similar results.

Biotinylation assays

Biotinylation pull down experiments were performed as described previously (Lobingier *et al*, 2017). Briefly biotinylation experiments were performed by transfecting GFP-Rab11-APEX2 constructs in to 2 million cells plated in 10-cm dishes. Cells were pre-incubated (40 min) with biotin phenol (Iris Biotech), after stimulation with ligands, hydrogen peroxide (Sigma-Aldrich) was added for 1 min before quenching with Trolox (Sigma-Aldrich) and sodium ascorbate (VWR) during ice-cold lysis. A 2-hour RT pull down with streptavidin beads was then performed running the supernatant against the bound proteins.

Proliferation assays

Incucyte cell proliferation assay

Indicated cell lines were seeded into 24-well plates at a density of 15,000–20,000 cells per well, depending on growth rate and the design of the experiment. After plating cells were starved and stimulated with indicated ligands every 24 h and imaged every hour using the Incucyte ZOOM (Essen Bioscience), phase-contrast images were analysed to detect cell proliferation based on cell confluence. And average confluency value over 4 h was used to determine the starting confluency from which a relative growth change was calculated. Statistical analysis was performed at the endpoint across repeats, as indicated in the Fig legends.

Crystal Violet

Indicated cells were stained after experimentation by being fixed with 0.5% w/v crystal violet (Sigma) in 4% w/v paraformaldehyde/PBS for 30 min. Fixed cells were then solubilized in 2% w/v SDS/PBS and absorbance measured at 595 nm using Synergy H1 microplate reader (BioTek). Statistical analysis was performed at the endpoint across repeats, as indicated in the Fig legends.

EdU incorporation

Indicated cells were labelled with 20 μ M 5-ethynyl-2'-deoxyuridine (EdU) for 4 h and processed following the manufacturer's protocol (Click-iT[®] EdU Alexa Fluor[®] 488 Imaging Kit, Thermo Fisher). Prior to imaging, cells were then stained with 5 ng/ml Hoechst 3342 for 15 min. Stained cells were analysed using a Leica microscope system. Statistical analysis was performed at the endpoint across repeats, as indicated in the Fig legends.

Invasion assay

Rat tail-derived collagen I (Corning) was supplemented with 25 μ g/ml human fibronectin (Sigma) in DMEM and polymerized in 8- μ m Transwell inserts (Corning) for 30 min at room temperature followed by 30 min at 37°C/5% CO₂. 5 x 10⁴ BT20 cells were seeded on the reverse of each insert and incubated for 6 h at 37°C/5% CO₂. Inserts were gently washed and placed in serum-free DMEM and the upper

chamber filled with DMEM supplemented with 10% FCS (Life Technologies) and either PBS or 100 ng/ml FGF10 (PeproTech). After 72 h, cells were stained with 500 ng/ml Calcein AM (Thermo Fisher) for 1 h and visualized by Leica Sp8 inverted confocal microscopy in serial sections of 20 μ m. Fluorescence intensity of each section was determined using ImageJ v. 1.52p (Schindelin *et al*, 2012) and proportion of invading cells estimated by comparing the total intensity beyond 40 μ m with the total overall intensity per insert using GraphPad PRISM version 8.0.0. Statistical analysis was performed at the endpoint across repeats, as indicated in the Fig legends.

Immunofluorescence

Immunofluorescence staining was performed as previously described (Francavilla *et al*, 2016). To detect HA-FGFR2b or endogenous FGFR2, we incubated cells with 10 μ g/ml of anti-HA (Covance) or anti-FGFR2 antibody (Cell Signalling) for 45 minutes with gentle agitation. The binding of the antibody did not activate receptor signalling in untreated cells nor induced receptor internalization (see control cells in Fig 1), as previously reported (Francavilla *et al*, 2009). After stimulation, cells were incubated at 37°C for different time points. When indicated, each inhibitor was added prior stimulation. At each time point, non-permeabilized cells were either fixed to visualize the receptor on the cell surface (plasma membrane) or acid-washed in ice-cold buffer (50 mM glycine, pH 2.5) to remove surface-bound antibody. Acid-washed cells were then fixed and permeabilized to visualize the internalized receptor (cytoplasm). Finally, to detect FGFR2b cells were stained with AlexaFluor488-conjugated donkey anti-mouse or anti-rabbit (Jackson ImmunoResearch Laboratories). Nuclei were stained with DAPI. Coverslips were then mounted in mounting medium (Vectashield; Vector Laboratories).

For co-localization experiments, cells were acid-washed, fixed, permeabilized with 0.02% saponin (Sigma), treated with a primary antibody against FGFR2, EGFR, TTP, RCP, phosphorylated T693 EGFR, EEA1 for 60 min at 37 °C and stained with AlexaFluor488 (or 568 or 647)-conjugated donkey anti-mouse or anti-rabbit. Samples either expressing GFP-tagged proteins or treated with TRITC-transferrin or Alexa 647-transferrin (to stain transferrin receptor, TfR), added to the medium at a final concentration of 50 μ g/mL, were kept in the dark. Nuclei were stained with DAPI. Coverslips were then mounted in mounting medium (Vectashield; Vector Laboratories).

All the images were acquired at room temperature on a Leica TCS SP8 AOBS inverted confocal using a 100x oil immersion objective and 2.5x confocal zoom. The confocal settings were as follows: pinhole, 1 airy unit, format, 1,024 x 1,024. Images were collected using the following detection mirror settings: FITC 494-530nm; Texas red 602-665nm; Cy5 640-690nm. The images were collected sequentially. Raw images were exported as.lsm files, and adjustments in image contrast and brightness were applied identical for all images in a given experiment using the freely available software ImageJ v. 1.52p (Schindelin *et al*, 2012).

Quantification of the recycling assay

Quantification of recycling was performed as described (Francavilla *et al*, 2016). For each time point and each treatment, the presence (total) and the localization (cell surface versus internalized) of HA-FGFR2 or endogenous FGFR2 were assessed in at least seven randomly chosen fields. Approximately 100 cells per condition (both acid-washed and not) were analysed from three independent

experiments. The results are expressed as the percentage of receptor-positive cells (green) over total cells (corresponding to DAPI-stained nuclei) and referred to the values obtained at time zero. Statistical analysis was performed across repeats, as indicated in the Fig legends.

Quantification of expression fraction, overlap fraction and co-localization

Images were pre-processed using an “À trous” wavelet band-pass filter to reduce the contribution of high-frequency speckled noise to the co-localization calculations. Pixel intensities were then normalized from the original 8-bit range [0,255] to [0,1]. To ensure that co-localization was only computed in well-determined regions of interest (ROI), we used the Fiji/ImageJ (Schindelin *et al*, 2012) built-in ROI manager to create and record these regions.

To measure differences in expression over time or between conditions, we computed the fractions of expressed red marker (R), green marker G, or far-red marker F, pixels over a region of interest (N_R , N_G or N_F pixels with a strictly positive intensity in N pixels):

$$F_R = \frac{N_R}{N} \quad F_G = \frac{N_G}{N} \quad F_F = \frac{N_F}{N}$$

To quantify the overlap fraction between two (R and G) or three (R, F and G) markers, we first multiplied the (normalized) channel intensities together, i.e. $I_{RG} = I_R \times I_G$ and $I_{RFG} = I_R \times I_F \times I_G$ to compute a new image whose intensity increases to 1 where the markers strongly overlap and decreases or becomes null for non-overlapping pixels. Our overlap fraction coefficient (OF) becomes the fraction of strictly positive pixels in the combined image over the number of pixels in the region of interest.

$$OF_{RG} = \frac{N_{RG}}{N} \quad OF_{RF} = \frac{N_{RF}}{N} \quad OF_{RFG} = \frac{N_{RFG}}{N}$$

Finally, to quantify the actual level of co-localization between two markers (e.g. R and G), we used the Manders co-localization coefficients (MCC) M1 and M2 (Manders *et al*, 1996). M1 measures the fraction of the R marker in compartments that also contain the G marker, and M2, the fraction of the G marker in compartments that also contain the R marker. Lower-bound thresholds for pixel intensities I_R and I_G were automatically determined using the Costes method (Costes *et al*, 2004).

Briefly,

$$M1 \cong \frac{\sum_{I_R > T_R} I_{R,C}}{\sum_{All I_R} I_R} \quad M2 \cong \frac{\sum_{I_C > T_C} I_{G,C}}{\sum_{All I_C} I_G}$$

where with T_R and T_G are the threshold set by the automated Costes algorithm for the R and G channels, and $I_{R,C}$ and $I_{G,C}$ pixels are co-localized if their intensity in the reciprocal channel is above T_R or T_G set for that channel.

To measure the simultaneous overlap of our three, red, far-red and green markers (R, F, G), we first used the overlap image between marker R and marker F as defined above (i.e. $I_{F,R} = I_F \times I_R$). We then measured the MCC co-localization parameter of this combined image against a Green marker using the MCC formulae above, together with the Costes method to determine the T_{FR} and T_C thresholds.

The scripts for the quantification of co-localization were written in the Python language, and the code for Costes-adjusted MCC was taken verbatim from the CellProfiler (McQuin *et al*, 2018) code base.

Student's t-test was subsequently used to determine the difference in pixel overlap fraction or Manders (Costes) coefficient between different experimental conditions in Figs 1 and Figs 5, and Appendix Fig S4 and S6.

Data availability

The mass spectrometry proteomics data in Thermo Scientific's *.raw format have been deposited to the ProteomeXchange Consortium via the PRIDE (Perez-Riverol *et al*, 2019) partner repository with the dataset identifier PXD018184. Submission details: Project Name: Proximal Phosphoproteomics Approaches revealed a FGFR-EGFR functional cross-talk Project accession: PXD018184. To download: <https://www.ebi.ac.uk/pride/archive/projects/PXD018184>. The scripts for the quantification of overlap fraction and co-localization are available on Github at the following address: https://github.com/manbio/smith_ferguson_coloc.

Expanded View for this article is available online.

Acknowledgements

We thank Profs. Lowe and Woodman, and Drs Caswell, Tournier and Lopez-Castejon for reading the manuscript and the Bioimaging and the Bio-MS Facilities (University of Manchester). Research in CF lab is supported by Wellcome Trust (WT Sir Henry Dale fellowship 107636/Z/15/Z), the Biotechnology and Biological Sciences Research Council (BB/R015864/1), and Medical Research Council (MR/T016043/1). PhD students are supported by BBSRC Doctoral Training Programme (HF and JW: BB/M011208/1); Wellcome Trust (CB: 210002/Z/17/Z); CR-UK Non-Clinical Training Award (JP: A27445); and NIHR Manchester Biomedical Research Centre non-clinical PhD Studentship (TK: IS-BRC-1215-20007). RBC is supported by Cancer Research UK and Breast Cancer Now (MAN-Q2-Y4/5).

Author contributions

MPS performed experiments, supervised HRF and helped writing the manuscript. HRF, JF, KMK, TK, CB, JP and SC performed experiments. EZ quantified imaging data. JW helped with data analysis. PF contributed to sample preparation for MS analysis. SW and DK performed the MS experiments and provided technical advice. RBC supervised TK. CF conceptualized the study, performed experiments, analysed the data, supervised PhD students and wrote the manuscript. All the authors contributed to writing and approving the manuscript.

Conflict of interest

The authors declare that they have no conflict of interest.

References

- Babina IS, Turner NC (2017) Advances and challenges in targeting FGFR signalling in cancer. *Nat Rev Cancer* 17: 318–332
- Barrow-McGee R, Kermorgant S (2014) Met endosomal signalling: in the right place, at the right time. *Int J Biochem Cell Biol* 49: 69–74
- Baumdick M, Bruggemann Y, Schmick M, Xouri G, Sabet O, Davis L, Chin JW, Bastiaens PI (2015) EGF-dependent re-routing of vesicular recycling

- switches spontaneous phosphorylation suppression to EGFR signalling. *Elife* 4: e12223
- Bergeron JJ, Di Guglielmo GM, Dahan S, Dominguez M, Posner BI (2016) Spatial and temporal regulation of receptor tyrosine kinase activation and intracellular signal transduction. *Annu Rev Biochem* 85: 573–597
- Boluday I, Aebersold R (2020) Proteomic and interactomic insights into the molecular basis of cell functional diversity. *Nat Rev Mol Cell Biol* 21: 327–340
- Bolstad BM, Irizarry RA, Astrand M, Speed TP (2003) A comparison of normalization methods for high density oligonucleotide array data based on variance and bias. *Bioinformatics* 19: 185–193
- Budick-Harmelin N, Miaczynska M (2018) Integration of the endocytic system into the network of cellular functions. *Prog Mol Subcell Biol* 57: 39–63
- Butti R, Das S, Gunasekaran VP, Yadav AS, Kumar D, Kundu GC (2018) Receptor tyrosine kinases (RTKs) in breast cancer: signalling, therapeutic implications and challenges. *Mol Cancer* 17: 34
- Cao X (2016) Self-regulation and cross-regulation of pattern-recognition receptor signalling in health and disease. *Nat Rev Immunol* 16: 35–50
- Caswell P, Norman J (2008) Endocytic transport of integrins during cell migration and invasion. *Trends Cell Biol* 18: 257–263
- Ceresa BP, Peterson JL (2014) Cell and molecular biology of epidermal growth factor receptor. *Int Rev Cell Mol Biol* 313: 145–178
- Cheng Y, Tian H (2017) Current development status of MEK inhibitors. *Molecules* 22: 1551
- Clayton NS, Grose RP (2018) Emerging roles of fibroblast growth factor 10 in cancer. *Front Genet* 9: 499
- Collinet C, Stöter M, Bradshaw CR, Samusik N, Rink JC, Kenski D, Habermann B, Buchholz F, Henschel R, Mueller MS et al (2010) Systems survey of endocytosis by multiparametric image analysis. *Nature* 464: 243–249
- Costes SV, Daelemans D, Cho EH, Dobbin Z, Pavlakis G, Lockett S (2004) Automatic and quantitative measurement of protein-protein colocalization in live cells. *Biophys J* 86: 3993–4003
- Coulouval K, Kooken H, Roger PP (2011) Coupling of T161 and T14 phosphorylations protects cyclin B-CDK1 from premature activation. *Mol Biol Cell* 22: 3971–3985
- Cox J, Hein MY, Luber CA, Paron I, Nagaraj N, Mann M (2014) Accurate proteome-wide label-free quantification by delayed normalization and maximal peptide ratio extraction, termed MaxLFQ. *Mol Cell Proteomics* 13: 2513–2526
- Cox J, Mann M (2008) MaxQuant enables high peptide identification rates, individualized p.p.b.-range mass accuracies and proteome-wide protein quantification. *Nat Biotechnol* 26: 1367–1372
- Cox J, Neuhauser N, Michalski A, Scheltema RA, Olsen JV, Mann M (2011) Andromeda: a peptide search engine integrated into the MaxQuant environment. *J Proteome Res* 10: 1794–1805
- Crupi MJF, Maritan SM, Reyes-Alvarez E, Lian EY, Hyndman BD, Rekab AN, Moodley S, Antonescu CN, Mulligan LM (2020) GGA3-mediated recycling of the RET receptor tyrosine kinase contributes to cell migration and invasion. *Oncogene* 39: 1361–1377
- Doll S, Gnad F, Mann M (2019) The case for proteomics and phospho-proteomics in personalized cancer medicine. *Proteomics Clin Appl* 13: e1800113
- Du Z, Lovly CM (2018) Mechanisms of receptor tyrosine kinase activation in cancer. *Mol Cancer* 17: 58
- Emami H, Vucic E, Subramanian S, Abdelbaky A, Fayad ZA, Du S, Roth E, Ballantyne CM, Mohler ER, Farkouh ME et al (2015) The effect of BMS-582949, a P38 mitogen-activated protein kinase (P38 MAPK) inhibitor on arterial inflammation: a multicenter FDG-PET trial. *Atherosclerosis* 240: 490–496
- Eyre R, Alférez DG, Spence K, Kamal M, Shaw FL, Simões BM, Santiago-Gómez A, Sarmiento-Castro A, Bramley M, Absar M et al (2016) Patient-derived mammosphere and xenograft tumour initiation correlates with progression to metastasis. *J Mammary Gland Biol Neoplasia* 21: 99–109
- Francavilla C, Cattaneo P, Berezin V, Bock E, Ami D, de Marco A, Christofori G, Cavallaro U (2009) The binding of NCAM to FGFR1 induces a specific cellular response mediated by receptor trafficking. *J Cell Biol* 187: 1101–1116
- Francavilla C, Papetti M, Rigbolt KT, Pedersen AK, Sigurdsson JO, Cazzamali G, Kæremore G, Blagoev B, Olsen JV (2016) Multilayered proteomics reveals molecular switches dictating ligand-dependent EGFR trafficking. *Nat Struct Mol Biol* 23: 608–618
- Francavilla C, Rigbolt K, Emdal K, Carraro G, Vernet E, Bekker-Jensen D, Streicher W, Wikström M, Sundström M, Bellusci S et al (2013) Functional proteomics defines the molecular switch underlying FGF receptor trafficking and cellular outputs. *Mol Cell* 51: 707–722
- Gan HK, Walker F, Burgess AW, Rigopoulos A, Scott AM, Johns TG (2007) The epidermal growth factor receptor (EGFR) tyrosine kinase inhibitor AG1478 increases the formation of inactive untethered EGFR dimers. Implications for combination therapy with monoclonal antibody 806. *J Biol Chem* 282: 2840–2850
- Gillingham AK, Bertram J, Begum F, Munro S (2019) In vivo identification of GTPase interactors by mitochondrial relocalization and proximity biotinylation. *Elife* 8: e45916
- Goh LK, Sorkin A (2013) Endocytosis of receptor tyrosine kinases. *Cold Spring Harb Perspect Biol* 5: a017459
- Gut C, Herrmann MD, Pelkmans L (2018) Multiplexed protein maps link subcellular organization to cellular states. *Science* 361: eaar7042
- Han Y, Caday CG, Nanda A, Cavenee WK, Huang HJ (1996) Tyrphostin AG 1478 preferentially inhibits human glioma cells expressing truncated rather than wild-type epidermal growth factor receptors. *Can Res* 56: 3859–3861
- Hanker AB, Garrett JT, Estrada MV, Moore PD, Ericsson PG, Koch JP, Langley E, Singh S, Kim PS, Frampton GM et al (2017) HER2-overexpressing breast cancers amplify FGFR signalling upon acquisition of resistance to dual therapeutic blockade of HER2. *Clin Cancer Res* 23: 4323–4334
- Harbeck N, Penault-Llorca F, Cortes J, Gnant M, Houssami N, Poortmans P, Ruddy K, Tsang J, Cardoso F (2019) Breast cancer. *Nat Rev Dis Primers* 5: 66
- Haugsten EM, Sorensen V, Brech A, Olsnes S, Wesche J (2005) Different intracellular trafficking of FGF1 endocytosed by the four homologous FGF receptors. *J Cell Sci* 118: 3869–3881
- Heisermann GJ, Wiley HS, Walsh BJ, Ingraham HA, Fiol CJ, Gill GN (1990) Mutational removal of the Thr669 and Ser671 phosphorylation sites alters substrate specificity and ligand-induced internalization of the epidermal growth factor receptor. *J Biol Chem* 265: 12820–12827
- Huang K-L, Li S, Mertins P, Cao S, Gunawardena HP, Ruggles KV, Mani Dr, Clauser KR, Tanioka M, Usary J et al (2017) Proteogenomic integration reveals therapeutic targets in breast cancer xenografts. *Nat Commun* 8: 14864
- Huang PH (2012) Phosphoproteomic studies of receptor tyrosine kinases: future perspectives. *Mol Biosyst* 8: 1100–1107
- Issa A, Gill JW, Heideman MR, Sahin O, Wiemann S, Dey JH, Hynes NE (2013) Combinatorial targeting of FGF and ErbB receptors blocks growth and metastatic spread of breast cancer models. *Breast Cancer Res* 15: R8
- Kobayashi Y, Lim SO, Yamaguchi H (2020) Oncogenic signalling pathways associated with immune evasion and resistance to immune checkpoint inhibitors in cancer. *Semin Cancer Biol* 65: 51–64

- Lanzetti L, Di Fiore PP (2017) Behind the scenes: endo/exocytosis in the acquisition of metastatic traits. *Can Res* 77: 1813–1817
- Lemmon MA, Schlessinger J (2010) Cell signalling by receptor tyrosine kinases. *Cell* 141: 1117–1134
- Liao Y, Wang J, Jaehnig EJ, Shi Z, Zhang B (2019) WebGestalt 2019: gene set analysis toolkit with revamped UIs and APIs. *Nucleic Acids Res* 47: W199–W205
- Liberali P, Snijder B, Pelkmans L (2014) A hierarchical map of regulatory genetic interactions in membrane trafficking. *Cell* 157: 1473–1487
- Lobingier BT, Huttenhain R, Eichel K, Miller KB, Ting AY, von Zastrow M, Krogan NJ (2017) An approach to spatiotemporally resolve protein interaction networks in living cells. *Cell* 169: 350–360
- Lundby A, Franciosa G, Emdal KB, Refsgaard JC, Gnosa SP, Bekker-Jensen DB, Secher A, Maurya SR, Paul I, Mendez BL et al (2019) Oncogenic mutations rewire signalling pathways by switching protein recruitment to phosphotyrosine sites. *Cell* 179: 543–560
- Maennling AE, Tur MK, Niebert M, Klockenbring T, Zeppernick F, Gattenlohner S, Meinhold-Heerlein I, Hussain AF (2019) Molecular targeting therapy against EGFR family in breast cancer: progress and future potentials. *Cancers* 11: 1826
- Manders EM, Hoebe R, Strackee J, Vossepoel AM, Aten JA (1996) Largest contour segmentation: a tool for the localization of spots in confocal images. *Cytometry* 23: 15–21
- McQuin C, Goodman A, Chernyshev V, Kametsky L, Cimini BA, Karhohs KW, Doan M, Ding L, Rafelski SM, Thirstrup D et al (2018) Cell Profiler 3.0: Next-generation image processing for biology. *PLoS Biol* 16: e2005970
- Mellman I, Yarden Y (2013) Endocytosis and cancer. *Cold Spring Harb Perspect Biol* 5: a016949
- Mertins P, Mani Dr, Ruggles KV, Gillette MA, Clauser KR, Wang P, Wang X, Qiao JW, Cao S, Petralia F et al (2016) Proteogenomics connects somatic mutations to signalling in breast cancer. *Nature* 534: 55–62
- Navid S, Fan C, Flores-Villanueva PO, Generali D, Li Y (2020) The fibroblast growth factor receptors in breast cancer: from oncogenesis to better treatments. *Int J Mol Sci* 21: 2011
- Neve RM, Chin K, Fridlyand J, Yeh J, Baehner FL, Fevr T, Clark L, Bayani N, Coppe J-P, Tong F et al (2006) A collection of breast cancer cell lines for the study of functionally distinct cancer subtypes. *Cancer Cell* 10: 515–527
- Nguyen LK, Kholodenko BN (2016) Feedback regulation in cell signalling: Lessons for cancer therapeutics. *Semin Cell Dev Biol* 50: 85–94
- Olsen JV, Blagoev B, Gnand F, Macek B, Kumar C, Mortensen P, Mann M (2006) Global, in vivo, and site-specific phosphorylation dynamics in signalling networks. *Cell* 127: 635–648
- Ornitz DM, Itoh N (2015) The fibroblast growth factor signalling pathway. *Wiley Interdiscip Rev Dev Biol* 4: 215–266
- Pardo OE, Latigo J, Jeffery RE, Nye E, Poulson R, Spencer-Dene B, Lemoine NR, Stamp GW, Aboagye EO, Seckl MJ (2009) The fibroblast growth factor receptor inhibitor PD173074 blocks small cell lung cancer growth in vitro and in vivo. *Can Res* 69: 8645–8651
- Perez-Riverol Y, Csordas A, Bai J, Bernal-Llinares M, Hewapathirana S, Kundu DJ, Inuganti A, Griss J, Mayer G, Eisenacher M et al (2019) The PRIDE database and related tools and resources in 2019: improving support for quantification data. *Nucleic Acids Res* 47: D442–D450
- Pletscher-Frankild S, Palleja A, Tsafou K, Binder JX, Jensen LJ (2015) DISEASES: text mining and data integration of disease-gene associations. *Methods* 74: 83–89
- Porebska N, Latko M, Kucinska M, Zakrzewska M, Otlewski J, Opalinski L (2018) Targeting cellular trafficking of fibroblast growth factor receptors as a strategy for selective cancer treatment. *J Clin Med* 8: 7
- R Core Team (2018) *R: A language and environment for statistical computing*. Vienna: R Foundation for Statistical Computing
- Sachs N, de Ligt J, Kopper O, Gogola E, Bounova G, Weeber F, Balgobind AV, Wind K, Gracanin A, Begthel H et al (2018) A living biobank of breast cancer organoids captures disease heterogeneity. *Cell* 172: 373–386
- Santiago-Gómez A, Kedward T, Simões BM, Dragoni I, NicAmhlaoibh R, Trivier E, Sabin V, Gee JM, Sims AH, Howell SJ et al (2019) PAK4 regulates stemness and progression in endocrine resistant ER-positive metastatic breast cancer. *Cancer Lett* 458: 66–75
- Schindelin J, Arganda-Carreras I, Frise E, Kaynig V, Longair M, Pietzsch T, Preibisch S, Rueden C, Saalfeld S, Schmid B et al (2012) Fiji: an open-source platform for biological-image analysis. *Nat Methods* 9: 676–682
- Schmid SL (2017) Reciprocal regulation of signalling and endocytosis: Implications for the evolving cancer cell. *J Cell Biol* 216: 2623–2632
- Shannon P, Markiel A, Ozier O, Baliga NS, Wang JT, Ramage D, Amin N, Schwikowski B, Ideker T (2003) Cytoscape: a software environment for integrated models of biomolecular interaction networks. *Genome Res* 13: 2498–2504
- Sharrocks AD (2006) Cell cycle: sustained ERK signalling represses the inhibitors. *Curr Biol* 16: R540–542
- Singhrrunnusorn P, Ueno Y, Matsuo M, Suzuki S, Saiki I, Sakurai H (2007) Transient suppression of ligand-mediated activation of epidermal growth factor receptor by tumor necrosis factor-alpha through the TAK1-p38 signalling pathway. *J Biol Chem* 282: 12698–12706
- Stallaert W, Bruggemann Y, Sabet O, Baak L, Gattiglio M, Bastiaens PIH (2018) Contact inhibitory Eph signalling suppresses EGF-promoted cell migration by decoupling EGFR activity from vesicular recycling. *Sci Signal* 11: eaat0114
- Szklarczyk D, Gable AL, Lyon D, Junge A, Wyder S, Huerta-Cepas J, Simonovic M, Doncheva NT, Morris JH, Bork P et al (2019) STRING v11: protein-protein association networks with increased coverage, supporting functional discovery in genome-wide experimental datasets. *Nucleic Acids Res* 47: D607–D613
- Tan AC, Vyse S, Huang PH (2017) Exploiting receptor tyrosine kinase co-activation for cancer therapy. *Drug Discov Today* 22: 72–84
- Tate JG, Bamford S, Jubb HC, Sondka Z, Beare DM, Bindal N, Boutselakis H, Cole CG, Creatore C, Dawson E et al (2019) COSMIC: the catalogue of somatic mutations in cancer. *Nucleic Acids Res* 47: D941–D947
- Tomas A, Vaughan SO, Burgoyne T, Sorkin A, Hartley JA, Hochhauser D, Futter CE (2015) WASH and Tsg101/ALIX-dependent diversion of stress-internalized EGFR from the canonical endocytic pathway. *Nat Commun* 6: 7324
- Tyanova S, Cox J (2018) Perseus: a bioinformatics platform for integrative analysis of proteomics data in cancer research. *Methods Mol Biol* 1711: 133–148
- Uhlitz F, Sieber A, Wyler E, Fritsche-Guenther R, Meisig J, Landthaler M, Klinger B, Bluthgen N (2017) An immediate-late gene expression module decodes ERK signal duration. *Mol Syst Biol* 13: 944
- Watson J, Francavilla C (2018) Regulation of FGF10 signalling in development and disease. *Front Genet* 9: 500
- Weber F, Fukino K, Sawada T, Williams N, Sweet K, Brena RM, Plass C, Caldes T, Mutter GL, Villalona-Calero MA et al (2005) Variability in organ-specific EGFR mutational spectra in tumour epithelium and stroma may be the biological basis for differential responses to tyrosine kinase inhibitors. *Br J Cancer* 92: 1922–1926

- Winograd-Katz SE, Levitzki A (2006) Cisplatin induces PKB/Akt activation and p38(MAPK) phosphorylation of the EGF receptor. *Oncogene* 25: 7381–7390
- Wintheiser GA, Silberstein P (2020) *Physiology, Tyrosine Kinase Receptors*. Treasure Island, FL: StatPearls
- Wittkowski KM, Dadurian C, Seybold MP, Kim HS, Hoshino A, Lyden D (2018) Complex polymorphisms in endocytosis genes suggest alpha-cyclodextrin as a treatment for breast cancer. *PLoS One* 13: e0199012
- Wu X, Zahari MS, Renuse S, Sahasrabudhe NA, Chaerkady R, Kim M-S, Fackler MJ, Stampfer M, Gabrielson E, Sukumar S et al (2018) Quantitative phosphoproteomic analysis reveals reciprocal activation of receptor tyrosine kinases between cancer epithelial cells and stromal fibroblasts. *Clin Proteomics* 15: 21
- Yaffe MB (2019) Why geneticists stole cancer research even though cancer is primarily a signalling disease. *Sci Signal* 12: eaaw3483
- Zakrzewska M, Haugsten EM, Nadratowska-Wesolowska B, Oppelt A, Hausott B, Jin Y, Otlewski J, Wesche J, Wiedlocha A (2013) ERK-mediated phosphorylation of fibroblast growth factor receptor 1 on Ser777 inhibits signalling. *Sci Signal* 6: ra11
- Zinkle A, Mohammadi M (2019) Structural biology of the FGF7 subfamily. *Front Genet* 10: 102
- Zwang Y, Yarden Y (2006) p38 MAP kinase mediates stress-induced internalization of EGFR: implications for cancer chemotherapy. *EMBO J* 25: 4195–4206



License: This is an open access article under the terms of the Creative Commons Attribution License, which permits use, distribution and reproduction in any medium, provided the original work is properly cited.